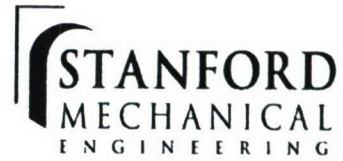


REPORT DOCUMENTATION PAGE

AFRL-SR-AR-TR-07-0078

Public reporting burden for this collection of information is estimated to average 1 hour per response, including the time for reviewing instructions, searching existing data sources, gathering the data needed, and completing and reviewing this collection of information. Send comments regarding this burden estimate or any other aspect of this collection of information, including suggestions for reducing this burden, to Washington Headquarters Services, Directorate for Information Operations and Reports (0704-0188), 1215 Jefferson Davis Boulevard, Arlington, VA 22202-4302. Respondents should be aware that notwithstanding any other provision of law, no person shall be subject to any penalty for failing to comply with a collection of information if it does not display a valid OMB control number. PLEASE DO NOT RETURN YOUR FORM TO THE ABOVE ADDRESS.

1. REPORT DATE (DD-MM-YYYY) 30-01-2007		2. REPORT TYPE Final Technical		3. DATES COVERED (From - To) 01-11-2003 - 31-10-2006	
4. TITLE AND SUBTITLE (U) Laser Diagnostics for Reacting Flows				5a. CONTRACT NUMBER	
				5b. GRANT NUMBER FA9550-04-1-0009	
				5c. PROGRAM ELEMENT NUMBER 61102F	
6. AUTHOR(S) Ronald K. Hanson				5d. PROJECT NUMBER 2308	
				5e. TASK NUMBER BX	
				5f. WORK UNIT NUMBER	
7. PERFORMING ORGANIZATION NAME(S) AND ADDRESS(ES) Stanford University 651 Serra Street Stanford CA 94305				8. PERFORMING ORGANIZATION REPORT NUMBER	
				10. SPONSOR/MONITOR'S ACRONYM(S)	
9. SPONSORING / MONITORING AGENCY NAME(S) AND ADDRESS(ES) AFOSR/NA 875 North Randolph Street Suite 325, Room 3112 Arlington VA 22203-1768 <i>Dr. Julian Tishkoff/NA</i>				11. SPONSOR/MONITOR'S REPORT NUMBER(S)	
12. DISTRIBUTION / AVAILABILITY STATEMENT Approved for public release; distribution is unlimited					
13. SUPPLEMENTARY NOTES					
14. ABSTRACT Advanced optical diagnostic techniques relevant to propulsion were investigated. The techniques studied were based on laser spectroscopy, with emphasis on spectrally-resolved absorption and laser-induced fluorescence (LIF). Laser sources included tunable cw near-infrared diode lasers and tunable (or fixed-wavelength) pulsed lasers operated at ultraviolet (UV) or infrared (IR) wavelengths. The cw lasers were spectrally narrow, allowing study of innovative diagnostics based on spectral lineshapes, while the pulsed lasers provided intense bursts of photons needed for techniques based on LIF. Accomplishments of note included: (1) development of a new imaging diagnostic based on infrared planar laser-induced fluorescence (IR PLIF), (2) investigations of quantitative ultraviolet (UV) PLIF of NO and CO ₂ in high-pressure combustion environments, (3) the development of a new temperature diagnostic using UV absorption of CO ₂ for high-temperature combustion environments, (4) development of advanced wavelength-multiplexed diode laser absorption sensing of non-uniform temperature distributions, gas temperature in scramjet flows, and tunable mid-IR-based fuel sensing, and (5) further development of quantitative tracers to image fuel distribution using ketones and the aromatic toluene. The full spectrum of results was published in thirty-eight papers in the AIAA and peer reviewed literature, seven PhD theses, and forty-three presentations and invited lectures.					
15. SUBJECT TERMS Laser Diagnostics, Combustion, Propulsion, Absorption, Fluorescence, Temperature, High Pressure					
16. SECURITY CLASSIFICATION OF:			17. LIMITATION OF ABSTRACT UL	18. NUMBER OF PAGES 72	19a. NAME OF RESPONSIBLE PERSON Julian M. Tishkoff
a. REPORT Unclassified	b. ABSTRACT Unclassified	c. THIS PAGE Unclassified			19b. TELEPHONE NUMBER (include area code) (703) 696-8478



Final Technical Report

**LASER DIAGNOSTICS FOR REACTING
FLOWS**

Grant AFOSR FA9550-04-0009

DISTRIBUTION STATEMENT A
Approved for Public Release
Distribution Unlimited

Prepared for
Air Force Office of Scientific Research
Dr. Julian Tishkoff, Technical Monitor

For the Period
November 1, 2003 to October 31, 2006

Submitted by
Professor Ronald K. Hanson, Principal Investigator

HIGH TEMPERATURE GASDYNAMICS LABORATORY
Mechanical Engineering Department
Stanford University, Stanford CA 94305

**H
T
G
L**

Table of Contents

1.0	Introduction.....	4
2.0	Project Summaries.....	5
2.1	Infrared PLIF imaging diagnostics.....	6
2.2	Quantitative LIF and PLIF measurements in high pressure-flames.....	13
2.2.1	Strategies for quantitative NO LIF.....	13
2.2.2	First PLIF imaging of CO ₂	19
2.3	Temperature diagnostics based on CO ₂ absorption of UV light.....	24
2.4	Advanced wavelength-multiplexed diode laser absorption diagnostics.....	30
2.4.1	Non-uniform temperature distributions.....	30
2.4.2	Scanned-wavelength modulation for high SNR absorption.....	42
2.4.3	Mid-IR measurements of fuels using diode lasers.....	52
2.5	Photophysics studies in support of tracers for fuel imaging.....	57
3.0	Publications and Presentations.....	61
4.0	Personnel.....	68
5.0	Technology Transitions/Transfers.....	69
5.1	Interactions and collaboration with AFRL	69
5.2	Transitions.....	70
8.0	Inventions or Patent Disclosures.....	72
9.0	Honors/Awards.....	72

1.0 Introduction

Advanced optical diagnostic techniques relevant to propulsion are investigated. The techniques studied are based on laser spectroscopy, with emphasis on spectrally-resolved absorption and laser-induced fluorescence (LIF). Laser sources include tunable cw near-infrared diode lasers and tunable (or fixed-wavelength) pulsed lasers operated at ultraviolet (UV) or infrared (IR) wavelengths. The cw lasers are spectrally narrow, allowing study of innovative diagnostics based on spectral lineshapes, while the pulsed lasers provide intense bursts of photons needed for techniques based on LIF. Accomplishments of note include: (1) development of a new imaging diagnostic based on infrared planar laser-induced fluorescence (IR PLIF), (2) investigations of quantitative ultraviolet (UV) PLIF of NO and CO₂ in high-pressure combustion environments, (3) the development of a new temperature diagnostic using UV absorption of CO₂ for high-temperature combustion environments, (4) development of advanced wavelength-multiplexed diode laser absorption sensing of non-uniform temperature distributions, gas temperature in scramjet flows, and tunable mid-IR-based fuel sensing, and (5) further development of quantitative tracers to image fuel distribution using ketones and the aromatic toluene. The full spectrum of results is published in thirty-eight papers in the AIAA and peer reviewed literature, seven PhD theses, and forty-three presentations and invited lectures.

2.0 Project Summaries

2.1 Infrared PLIF imaging diagnostics

Infrared planar laser-induced fluorescence (IRPLIF) of carbon dioxide (CO_2) has been demonstrated in the past [2.1.1-4; e.g. see Refs. 1-4 at the end of section 2.1] for imaging room temperature and elevated temperature jets. The technique has also been used for imaging the fuel region of a laminar CO diffusion flame, and the nascent formation of CO_2 in a laminar methane diffusion flame [2.1.2,3]. In the current project, we extend this technique for the first time to supersonic flows, using IRPLIF of CO_2 to image the exit region of an underexpanded jet.

Background

IRPLIF involves the excitation of molecular vibrational modes via infrared laser radiation (an excitation wavelength of $2.0 \mu\text{m}$ is used for this work), followed by imaging of the subsequent vibrational fluorescence (fluorescence is collected from the $4.3 \mu\text{m}$ band of CO_2). Continued improvement in infrared laser sources and infrared camera technology make IRPLIF a competing method with UV/visible tracer PLIF for visualization of flows. IRPLIF offers the advantage, in some instances, of not needing to add a tracer to the flow if molecules with an IR-active vibrational mode, such as CO_2 , are naturally present in sufficient abundance. Even in situations where they need to be added, small molecules with IR-active vibrational modes offer the advantage of being gaseous under room temperature conditions. This reduces experimental complexity by doing away with the need to seed vapors from a liquid into a gaseous flow. Additionally, for applications in air-based systems, these molecules have small impact on the properties of the fluid being visualized because their molecular weights and specific heats are close to those of molecular oxygen, molecular nitrogen, and water.

The sub-atmospheric pressure regime, which is particularly important for high-speed flows, offers additional advantages for IRPLIF. Electronic PLIF can be dominated by collisionless nonradiative decay processes [2.1.5], however, for IRPLIF of small molecules, e.g. CO_2 , the only nonradiative deactivation processes present are due to collisions. Because the deactivation processes involve collisions, the deactivation rates are linearly proportional to the number density of the colliding species. Reducing the pressure of the environment to be imaged reduces the deactivation rate of the fluorescence, and increases the fluorescence quantum yield. For high-speed flows this advantage may be limited by the tolerable exposure time for the flow of interest. Typical deactivation times for vibrational fluorescence are on the order of microseconds for ambient temperature and pressure conditions. By contrast, lifetimes of nanoseconds or picoseconds are typical for electronic fluorescence so the motion of the flow is easily frozen. IRPLIF imaging in supersonic and hypersonic applications may thus require the sacrifice of signal level to achieve short integration times necessary to freeze the flow motion. The following sub-sections present IRPLIF theory and analysis as well as the experimental setup and imaging results for an underexpanded jet of CO_2 .

IRPLIF Theory and Analysis

The fluorescence equation in the linear excitation limit can be written as[2.1.5]

$$S_f = \frac{E}{h\nu_0} dV_c \frac{\chi_{abs} P}{kT} \sigma(P, T, g(\nu)) \phi(P, T, \chi_i) \eta_{coll} \quad (2.1.1)$$

where S_f is the number of photons per pixel incident on the camera, E is the laser fluence [J/cm^2], h is Planck's constant [$\text{J}\cdot\text{s}$], ν_0 is the center frequency of the laser [$1/\text{s}$], dV_c is the volume of the pixel in the laser sheet [cm^3], χ_{abs} is the mole fraction of the species being excited, P is the local pressure [MPa], k is the Boltzmann constant [J/K], T is the local temperature [K], $g(\nu)$ is the laser lineshape function [s], $\sigma(P, T, g(\nu))$ is the absorption cross section of the species being excited [cm^2], ϕ is the fluorescence quantum yield (FQY) which depends upon the local pressure, temperature, and species mole fractions (χ_i), and η_{coll} is the optical collection efficiency which includes transmission efficiencies of the optics and transmission of the fluorescence through the gas (radiative trapping influence) as well as the collection efficiency of the optics.

Quantities of key interest in Eqn. (2.1.1) are the absorbing species mole fraction, the local pressure, and the local temperature. The absorption cross section and FQY are important because they are dependent upon the quantities of interest and influence the signal level of the measurements. In supersonic flows, the pressure, temperature, and mole fraction are nonuniform, necessitating modeling of the functional dependence of the absorption cross section and FQY to determine the dependence of the fluorescence on these quantities.

Model Results

The absorption cross section is dependent upon temperature through the Boltzmann fraction in the rotational line being excited, as well as through the temperature dependence of the absorption lineshape due to collision broadening and Doppler broadening. The pressure dependence of the cross section arises due to the influence of collision broadening. In addition, to these influences, the cross section depends upon the convolution of the absorption and laser lineshapes. Absorption cross sections are calculated using line parameters from the HITRAN database and fitting them with Voigt profiles. These lineshapes are then convolved with the laser lineshape which is modeled as Lorentzian with a FWHM of 500 MHz based on the manufacturer's specifications. Cross sections are calculated over a two-dimensional range of temperature and pressure for multiple possible excitation wavelengths. The plots of absorption cross section are then used as an aid in selecting excitation wavelengths.

The definition of FQY for IRPLIF differs slightly from that for electronic PLIF due to the longer fluorescence lifetimes associated with infrared fluorescence. For IRPLIF the fluorescence lifetime is often longer than the camera integration time so the FQY is defined as an integration of the spontaneous emission rate, from the states emitting into the wavelength collection band of the camera, normalized by the total number of photons absorbed.

The deactivation of the excited vibrational population is due almost completely to collisions, although a small contribution is due to the fluorescence itself. For the small molecules that we are treating here, collisions are the mechanism by which vibrational energy is transferred between molecules (intermolecular) and between modes of a

molecule (intramolecular). Assuming translational and rotational equilibrium the problem reduces to finding the time-dependent population of each vibrational state for the molecules in the mixture of interest. The approach taken utilizes the master equation formalism where the population evolution in each state has the following form [2.1.6]

$$\frac{dn_{v,s}(t)}{dt} = K_{VV,intra} + K_{VV,inter} + K_{VV,sk} + K_{VT} + K_{A_{ij}} + K_{pump} \quad (2.1.2)$$

where $n_{v,s}$ is the time-dependent population in vibrational state v of molecule s , $K_{VV,intra}$ is the sum of intramodal vibration-to-vibration (VV) transfer rates into the vibrational state v , $K_{VV,inter}$ is the sum of the intermodal VV transfer rates into the vibrational state v , $K_{VV,sk}$ is the sum of the intermolecular VV transfer rates into the vibrational state v for collision between molecules of type s and molecules of type k , K_{VT} is the sum of the vibration-to-translation (VT) relaxation rates, $K_{A_{ij}}$ is the sum of the spontaneous emission rates into state v , and K_{pump} is the laser pumping rate into the state v , which is zero for states not coupled by the laser radiation. To solve for the time evolution of population in each of the vibrational states, state-to-state vibrational transfer rates are needed for each energy transfer process. For the model used for these calculations it is assumed that only single quantum transfers are significant, which is a good assumption for the relatively low levels of vibrational excitation expected. To maximize the use of available vibrational transfer rate information, rate parameterizations are used for the intramodal VV and VT processes. The parameterization used for the VV processes follows the method of Kurnosov et al[2.1.7]. Those used for VT processes follows the work of Dunnwald et al[2.1.6]. The parameterizations are fits to the available transfer rate data using analytical expressions based on modified forms of SSH theory.

Results of the master equation vibrational transfer model give the vibrational population as a function of time. With knowledge of the states emitting within the collection bandwidth of the camera, and the Einstein A coefficients for those states, the FQY can be obtained to the model results. To aid in the design of experiments the model is run for a range of temperature and pressure conditions resulting in a two-dimensional map of FQY.

CO₂ Fluorescence Pressure and Temperature Dependence

The dependence of the CO₂ fluorescence on pressure and temperature can be determined by substituting the modeling results into Eqn. (2.1.1). To simplify this process we can rewrite Eqn. (2.1.1) as follows

$$S_f = C \frac{\chi_{abs} P}{kT} \sigma(P, T, g(\nu)) \phi(P, T, \chi_i) \quad (2.1.3)$$

where C is a constant that can be determined through calibration with a known concentration of CO₂. Equation (2.1.3) indicates that we can elucidate the temperature and pressure dependencies of the fluorescence signal by plotting the product of the absorbing species number density, the absorption cross section, and the fluorescence quantum yield. Figure (2.1.1) shows a plot of this product as a function of temperature and pressure for pure CO₂. The temperature and pressure dependence of the fluorescence is relatively small over a large portion of the temperature and pressure range, indicating that the excitation frequency used in the plot would be a good choice for imaging the

species mole fraction. We can eliminate the dependence on local mole fraction by taking the ratio of an offset-wavelength excited image and a on-line-wavelength excited image.

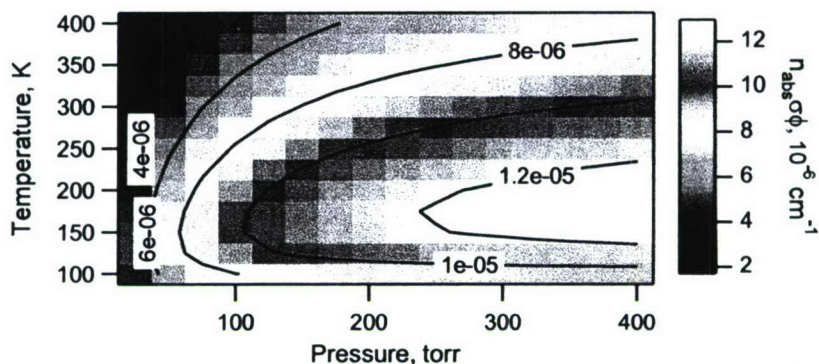


Figure 2.1.1. Temperature and pressure dependence of fluorescence from CO₂ as given by the product of the number density, absorption cross section, and fluorescence quantum yield. Excitation frequency of 4992.516 cm⁻¹.

Radiative Trapping

Infrared fluorescence is always resonant with an absorption band in the species from which the fluorescence originated; therefore, reabsorption of the fluorescence, in the mixture being excited, is always occurring to some extent. The reabsorption of fluorescence before it reaches the camera is known as radiative trapping. Trapping of the fluorescence has two main influences on the fluorescence signal, the first effect being a reduction in the signal intensity reaching the camera, and the second effect being the introduction of error in the measurement due to nonuniform trapping of the fluorescence across the field of view of the camera. Nonuniform trapping results from inhomogeneities in temperature, pressure, or species mole fraction between the plane of fluorescence emission and the plane of the imaging array.

For CO₂ radiative trapping often has significant influence especially when using 4.3 μm collection as is used in these experiments. This fluorescence corresponds to a $\Delta v = 1$ change in the ν_3 vibrational mode. This mode corresponds to the asymmetric stretching vibration of CO₂ which is one of the strongest transitions in the infrared spectral region. Even for the short distances used in this experiment, the influence of radiative trapping is significant. The trapping of the fluorescence will be nonuniform in this instance, as the edges of the jet have lower CO₂ concentration than the core of the jet; therefore, fluorescence from the edges is attenuated less than fluorescence from the core and the trapping will serve to augment the signal at the jet edges relative to the core. For imaging of CO₂ mole fraction this is problematic; however, for imaging of pressure or temperature using the ratio of two images this effect will cancel, and we can recover the pressure or temperature without the influence of nonuniform trapping.

Experimental Setup

A small vacuum tight cell with a converging nozzle mounted at the top is constructed to study an underexpanded CO₂ jet using IRPLIF. The nozzle for the jet is a 60° converging nozzle with an exit diameter of 1.5 mm. A pulsed solenoid valve is used to

turn the jet on and off. Images of the CO₂ jet injected into N₂ are acquired shortly after the pulsed solenoid valve opens. A plenum upstream of the pulsed valve is used to dampen out pressure fluctuation resulting from the opening of the valve. Capacitance manometers (Setra 280E) are used to monitor the pressure in the plenum and in the cell. The cell is connected to a gas-handling manifold allowing the cell to be filled with nitrogen prior to the CO₂ injection and the cell to be evacuated following the injection. The plenum pressure for the experiments is 1340 torr. The cell pressure is set to 170 torr. This gives a pressure ratio (p_{∞}/p_0) of 0.126 corresponding to a fully expanded Mach number of 2.0.

Laser excitation of CO₂ is provided by a OPO/OPA system (Continuum Mirage 3000) that has been modified with a second set of KTA crystals in the final amplifier stage to increase conversion efficiency [2.1.1]. The laser outputs pulses of approximately 20 mJ with a 4-6 ns FWHM duration at the target frequency of 4992.516 cm⁻¹. As discussed earlier, the spectral width of the laser is approximately 500 MHz FWHM. The laser beam is formed into a sheet using a combination of a 500 mm focal length spherical CaF₂ lens and a 250 mm focal length cylindrical CaF₂ lens. Placing the cylindrical lens 1000 mm after the focal point of the spherical lens produces a slightly diverging sheet height of 8.3 mm FWHM and a 400 μm FWHM waist.

Images are acquired with a LN₂ cooled InSb camera (Santa Barbara SBF134). The camera is outfitted with a wide bandpass (3.0-5.0 μm) interference filter with a transmission of approximately 90% over most of the transmission range. The filter provided high rejection of the scattered laser light, as well as rejection of some thermal background signal. A 25 mm diameter, 25 mm focal length CaF₂ singlet lens is used to focus the fluorescence onto the camera array, resulting in a magnification of 0.53. The pixel-by-pixel gain and offset of the camera with the filter and lens are calibrated by taking images of grey body emitters at several temperatures. The camera could be gated with integration times as small as 130 ns, and 300 ns integration times are used for this experiment.

Imaging Results

Images are taken using both the online-excitation and offset-excitation discussed earlier. Figure 2.1.2 shows a single-shot image of a pure CO₂ jet issuing into N₂ using online-excitation. The image has been corrected for background signal and the laser sheet profile and has been binned into two-pixel by two-pixel cells. Additionally, a three-pixel x three-pixel Gaussian filter is applied to smooth the data. As expected from the modeling for online excitation, we do not see significant fluctuation in signal corresponding to the pressure and temperature variations in the flow field. Instead, in the core of the jet, we see a relatively uniform signal over most of the image. Since online excitation is relatively insensitive to temperature and pressure, the signal reflects primarily changes in the CO₂ mole fraction. One notable exception is at the very top of the image, closest to the jet exit where the Riemann wave is located, where the significant variation in pressure and temperature cause a strong gradient to show up in the image.

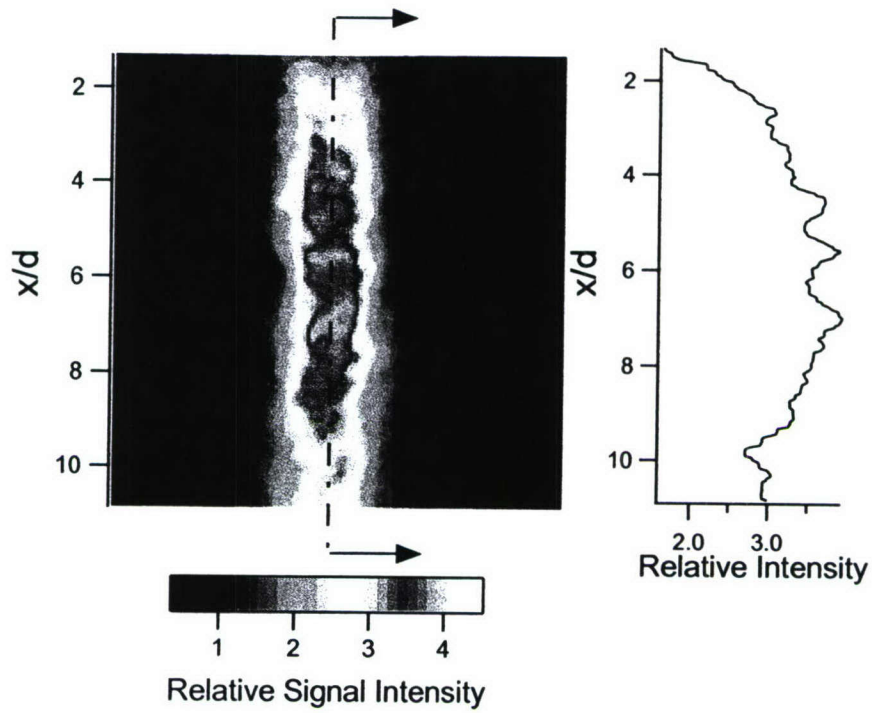


Figure 2.1.2. Online excitation image of a supersonic CO_2 jet into N_2 with a fully expanded Mach number of 2.0 issuing from a 1.5 mm diameter converging nozzle.

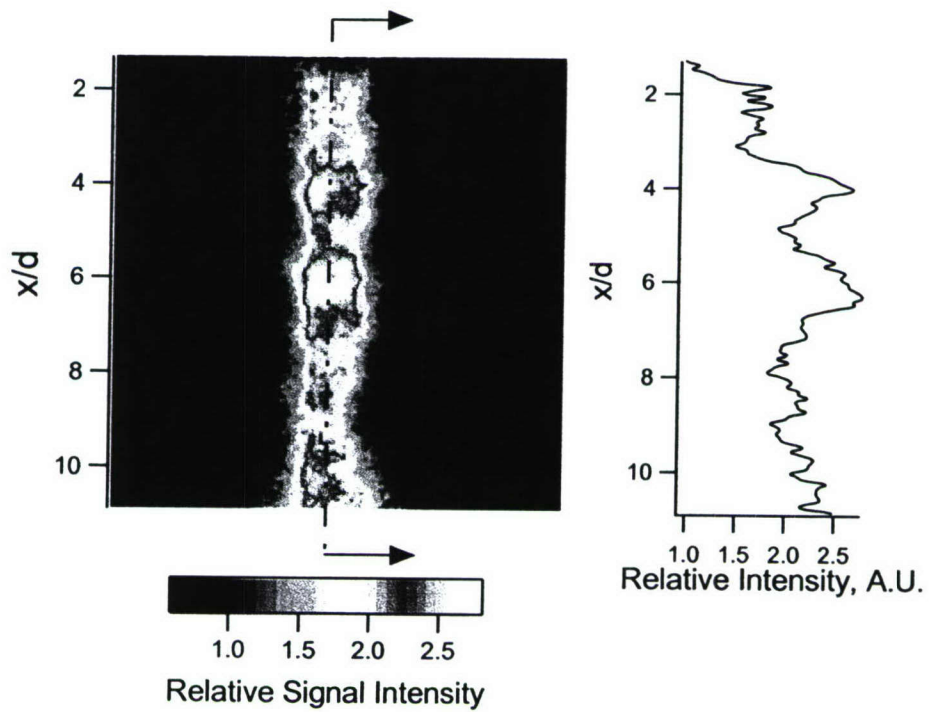


Figure 2.1.3. Offset excitation image of a supersonic CO_2 jet into N_2 with a fully expanded Mach number of 2.0 issuing from a 1.5 mm diameter converging nozzle.

An example single-shot image result for offset excitation is shown in Fig. 2.1.3. In this image, the pressure variations are readily apparent, along with the cellular nature of the jet. The signal reflects both variations in pressure, as well as CO₂ mole, with some dependence upon temperature and radiative trapping. To cancel the signal dependence upon CO₂ mole fraction and eliminate the trapping influence, we ratio the offset-excitation image by the online-excitation image. We can convert the data to pressure if we neglect the sensitivity to temperature and use an average value of temperature instead. Assuming an average temperature of 225 K, we obtain the pressure variation shown in Fig. 2.1.4.

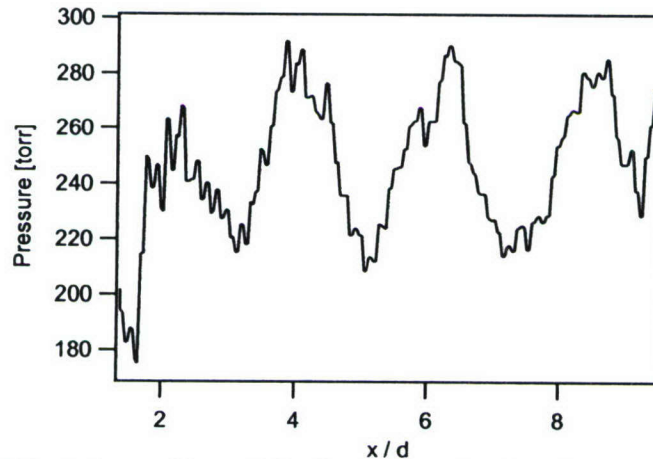


Figure 2.1.4. Estimated center line variation in pressure using the ratio of offset and online excitation images. Plot is generated using an average of ten images for both the offset and online images.

Current Status

A model for IRPLIF of CO₂ is developed and applied to optimize an imaging experiment for an underexpanded jet with a fully expanded Mach number of 2.0. Single-shot images of the jet are obtained using a 300 ns integration time. A technique is developed to measure pressure from the ratio of images of the jet excited at line center of the selected rotational transition with the laser detuned by 0.04 cm⁻¹. The ratio of these two images gives the local pressure with only small errors due to the temperature dependence of the fluorescence. To our knowledge, these images represent the first IRPLIF images of CO₂ in a supersonic flow. Future work will focus on further development of the technique. For example, by optimizing the excitation wavelengths it should be possible to reduce the temperature dependence further, or, by using the ratio of two images excited at different frequencies, the local static temperature in the supersonic flow could be determined. Recently, the infrared laser source has been improved, providing twice the excitation energy.

IRPLIF References

- [2.1.1] B.J. Kirby and R.K. Hanson, "Planar laser-induced fluorescence imaging of carbon monoxide using vibrational (infrared) transitions," *Applied Physics B-Lasers and Optics* **69** (1999) 505-507.
- [2.1.2] B.J. Kirby and R.K. Hanson, "Imaging of CO and CO₂ using infrared planar laser-induced fluorescence," *Proceedings of the Combustion Institute* **28** (2000) 253-259.
- [2.1.3] B.J. Kirby and R.K. Hanson, "CO₂ imaging with saturated planar laser-induced vibrational fluorescence," *Applied Optics* **40** (2001) 6136-6144.
- [2.1.4] B.J. Kirby and R.K. Hanson, "Linear excitation schemes for IR planar-induced fluorescence imaging of CO and CO₂," *Applied Optics* **41** (2002) 1190-1201.
- [2.1.5] M.C. Thurber, F. Grisch, B.J. Kirby, M. Votsmeier, R.K. Hanson, "Measurements and modeling of acetone laser-induced fluorescence with implications for temperature-imaging diagnostics," *Applied Optics* **37** (1998) 4963-4978.
- [2.1.6] Dunnwald, H., et al., "Anharmonic Vibration Vibration Pumping in Nitric-Oxide by Resonant Ir-Laser Irradiation," *Chemical Physics* **94** (1985) 195-213.
- [2.1.7] A. Kurnosov, M. Cacciatore, and G.D. Billings, "State-to-state rate constant calculations for V-V energy transfer in CO-N₂ collisions," *Journal of Physical Chemistry A* **107**(2003) 2403-2410.

2.2. Quantitative LIF and PLIF measurements of in high-pressure flames

Significant accomplishments are made in the development of diagnostic strategies and design rules for quantitative LIF and PLIF of NO in high pressure flames. In addition, the first UV-PLIF measurements are made on the combustion product CO₂, and this novel new diagnostic is demonstrated in the burnt gases of a high-pressure methane flame.

2.2.1 Strategies for quantitative NO LIF

Nitric oxide laser-induced-fluorescence (NO LIF) 2-D imaging in high-pressure flames (1–60bar) is investigated using a new multi-spectral detection strategy. This work builds on previous AFOSR-sponsored research that identified interference LIF from O₂ and CO₂ in high-pressure flames and optimized the choice of excitation strategies as a function of application conditions. The current work develops design rules to optimize the LIF detection wavelengths for quantitative 2-D NO-LIF measurements over a wide range of pressures and temperatures. Simultaneous detection of LIF in multiple wavelength regions enables correction of the NO signal for interference from O₂ and CO₂ and allows simultaneous imaging of all three species. New experiments of wavelength-resolved 1-D LIF in slightly lean ($\phi=0.9$) and slightly rich ($\phi=1.1$) methane/air flames are used to evaluate the design rules and estimate the NO detection limits for a wide range of flame conditions. The work done here provides a practical guideline for application of instantaneous 1-D or 2-D NO-LIF imaging strategies in high-pressure combustion systems.

Background

The elevated pressures of combustion environments in most practical systems introduce significant complications in the application of NO-LIF, as identified a decade ago [2.2.1]. Recently, with AFOSR support, we began a comprehensive study of quantitative NO-LIF in flames up to 60 bar, leading to enhanced understanding of high-pressure NO-LIF. Different *excitation* strategies are investigated and optimized excitation wavelengths for NO-LIF recommended for various combustion environments in a series of papers [2.2.2].

During the present grant, we investigated a new multi-spectral *detection* strategy for quantitative 2-D NO-LIF imaging. While the spectral analysis method is used routinely in bio-chemistry assays for complex polyatomic molecules, to our knowledge, this is the first application of multi-spectral detection in combustion LIF and certainly the first time for NO PLIF diagnostics. This work builds on the results of our previous efforts and leads to a new strategy based on the use of multiple detection wavelength regions for simultaneous determination of NO and the interference from O₂ and CO₂ LIF. Design rules are developed, and the detection wavelength regions or “windows” are optimized, using new wavelength-resolved 1-D NO-LIF experiments in slightly fuel lean ($\phi=0.9$) and slightly fuel rich ($\phi=1.1$) methane/air flames. Demonstration measurements of 2-D LIF imaging then are performed to validate the imaging strategy and estimate the NO detection limits for lean and rich high-pressure flames. Quantitative measurements of NO in these seeded flames are compared with detailed chemical kinetics calculations as a

function of pressure and stoichiometry, and good agreement is observed within the limits imposed on the calculation by the uncertainty in the measured temperature.

Experimental Details

The apparatus used in this study has been described previously [2.2.2] and only is discussed here briefly. Laminar, premixed methane/air flat-flames at pressures from 1 to 60 bar are stabilized on a porous, sintered stainless matrix of 8 mm diameter. This burner is mounted in a pressurized vessel with an inner diameter of 60 mm with stabilization to ± 0.1 bar. Investigations are conducted for $\phi=0.9$ and 1.1 methane/air equivalence ratios. Optical access to the flame is possible via four quartz windows (Heraeus, Suprasil 2 Grade). Laser pulse energy ranged from 0.8 to 1.2 mJ/pulse (7 ns pulse at 10 Hz with linewidth of 0.2 cm^{-1}) from a Nd:YAG-pumped (Quanta Ray GCR250) frequency-doubled (BBO) dye laser (LAS, LDL205). For spectrally resolved 1-D line imaging measurements, the beam is focused weakly (diameter = 1 mm) along a line 3 mm above the burner matrix and crosses the flame horizontally. The pulse energy is monitored with a fast photodiode (LaVision). Fluorescence signals are collected at right angles to the laser beam and focused with a $f = 105 \text{ mm}$, $f/4.5$ achromatic UV-lens (Nikon), dispersed spectrally through an imaging spectrometer (LaVision Chromex 250IS), and imaged onto an intensified CCD camera (LaVision Dynamight). For 2-D imaging measurements, the laser is stretched optically into a vertical sheet ($0.5 \text{ mm} \times 15 \text{ mm}$) and imaged directly using an ICCD camera with different filter sets for suppression of Rayleigh Scattering and bandpass filtering. The signals from 20 laser pulses are accumulated on chip for all measurements. For multi-window imaging measurements, wavelength regions are isolated with bandpass filters (discussed below) and separately collected on a single camera. For practical 2-D imaging applications where all spectral windows require simultaneous detection, a single laser, multi-camera strategy can be used.

Measurement Strategy

There are three significant complications that arise when applying NO-LIF to high-pressure combustion environments: (1) pressure broadening and shifting of NO transitions, (2) strong attenuation of UV light and (3) interference LIF. Excitation features of NO broaden with increased pressure, and for pressures greater than 10 bar, it is no longer possible to excite single rotational features of the excitation spectrum due to the spectral overlap [2.2.2]. Along with an increase in fluorescence quenching of the NO A state, pressure broadening leads to a decrease in the overall signal strength since the laser linewidth (0.2 cm^{-1}) is less than the broadened linewidths. Second is the strong attenuation effect of both the excitation laser light and fluorescence signal. UV light at short wavelengths ($<250 \text{ nm}$) is absorbed strongly in hot post-combustion gases, due mainly to strong absorption by CO_2 and H_2O [2.2.3] (CO_2 being the more dominant contributor in our wavelength range and temperatures). This effect increases with pressure as densities of the absorbing species increase. Finally, there can be significant signal interference. The $B^3\Sigma^- - X^3\Sigma^+$ Schumann-Runge bands of O_2 are pervasive in the same excitation and detection region and can be a major interference source in fuel lean and non-premixed flames [2.2.1]. Recently identified CO_2 broadband emission (200–450nm) is also a concern in high-pressure flames [2.2.4]. Additionally, polycyclic

aromatic hydrocarbon (PAH) LIF emission can be a source of significant interference in fuel-rich flames.

Isolation of NO-LIF signal from interference sources, mainly from LIF of hot O₂ and CO₂ is investigated using LIF detection in multiple wavelength windows, a novel concept in NO-LIF imaging. While an ultimate goal of our work is the development of a single-shot 2-D imaging strategy, all the data presented here are obtained by accumulating multiple laser pulses on an ICCD camera (20 shots/image), made possible by the steady nature of our test flame. By averaging over multiple laser pulses, we are able to estimate the single-shot LIF signals achievable using lasers above the modest power range (0.8 to 1.2 mJ/pulse) of our current setup. Figure 2.2.1 shows a typical emission spectrum of NO-LIF using 1-D imaging with *A-X(0,0)* band excitation, where non-linear fitting and computational simulation of NO, O₂, and CO₂ LIF emission are used to separate the spectrum into components from NO, O₂, and CO₂ LIF and the Rayleigh scattering of the laser. It can be seen that O₂ and CO₂ LIF are emitted throughout the entire region of interest and overlap with the spectral features of NO.

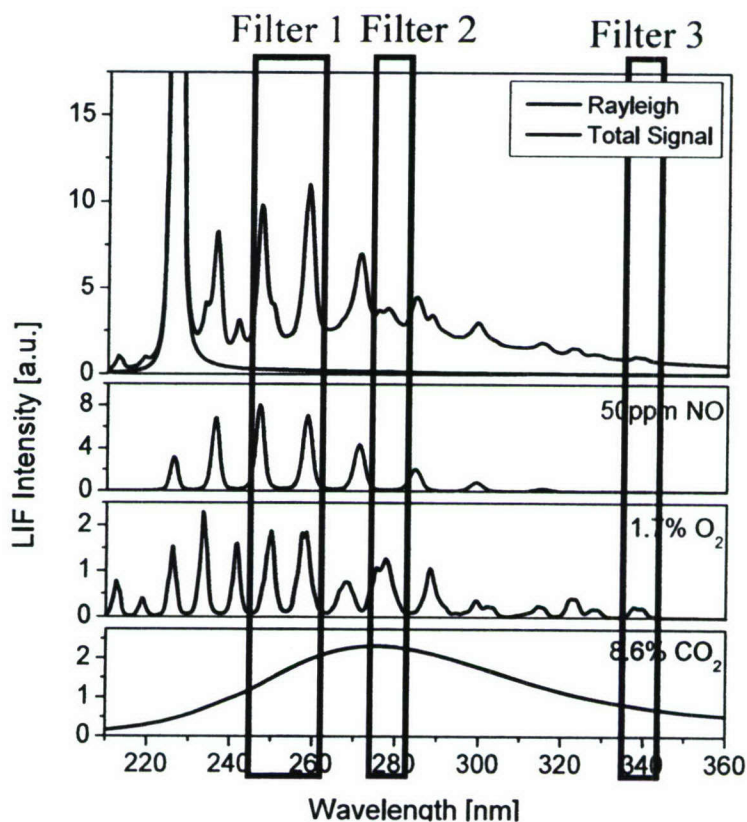


Figure 2.2.1. Emission Spectra of NO-LIF with 226.03nm Excitation (40bar flame, $\phi=0.9$, 300 ppm NO seeding). Spectra are obtained by taking 1-D line-imaging (top box). NO, O₂ and CO₂ emission profiles are enhanced for clarity (bottom 3 boxes). Filter 1, filter 2 and filter 3 indicate the detection windows. Profiles are taken in a 1mm region in the center of the flame.

Spectrally resolved 1-D imaging is obtained by aligning the laser beam parallel to the spectrometer slit, and the LIF signal is dispersed onto an ICCD camera. This camera image has the position along the laser beam on the ordinate and the fluorescence

wavelength on the abscissa. 1-D line-imaging provides increased signal-to-noise ratio (SNR) ratio due to higher laser intensity (beam vs. sheet), direct visualization of interference sources, and a more flexible selection of excitation/detection strategies, since NO-LIF can be isolated easily from interferences. In addition, only a single laser and single camera detection setup is required.

With modern-day high-power, short pulse (<10ns) lasers, LIF signal dependence on laser energy can show non-linear effects due to saturation of the excitation transition. In our 1-D line imaging experiments we observe only a slight deviation from linear excitation when the laser spectral intensity (I_ν) reach $\sim 30 \text{ W/m}^2\cdot\text{s}^{-1}$ (1 mJ, 7 ns pulse @ 226.03 nm with 0.2 cm^{-1} bandwidth and a focused diameter of 1 mm) in an atmospheric pressure flame. As pressure is increased to the pressures of current interest, the rapid increase in the rotational energy transfer refills the depleted ground state while removing excess population in the upper excited state, thereby greatly extending the linear regime of NO-LIF. This population recycling effect enables the use of higher laser power for linear single-shot imaging in high-pressure environments (e.g., up to 20 mJ/pulse @ 20 bar for our setup) resulting in increased SNR ratios. For 2-D imaging measurements, significantly stronger laser pulses can be used since the laser beam is dispersed into a sheet and the spectral intensity is decreased.

Experimental Results

Figure 2.2.1 shows the detection windows (filters) used for the 2-D imaging measurements. Filter 1 (254 nm, FWHM 17.5 nm; Asahi Optics) is the primary detection channel for NO, chosen to optimize the NO LIF signal, while filter 2 (280 nm, FWHM 12 nm; Lambda Research Optics) and filter 3 (340 nm, FWHM 10 nm; Asahi Optics) are used to correct the signal for interference from O_2 and CO_2 , respectively. In addition, a 240 nm long-pass filter is used for additional suppression of the Rayleigh scattering. The selection rules for filter 1, the primary NO-LIF detection window, maximize the selectivity and intensity while minimizing the contribution from Rayleigh scattering of the laser. The bandpass width also should be wide enough to avoid bias in the collection efficiency, depending on the rotational levels excited. For our test flame, optimization is carried out by taking the spectrally resolved line-imaged data (Fig. 2.2.1) and scanning a simulated Gaussian filter function (with varying spectral widths) throughout the fluorescence spectrum. For detection windows (filter 2 and filter 3) that are used to isolate interference LIF, the selection criteria require regions with maximum fractional contribution from the specific interference species for increased accuracy in the correction.

Selection of the optimum number of detection wavelength windows requires knowledge regarding the global chemistry of the combustion process involved. For many experimental applications, single-window detection (filter 1) is sufficient, as the flames have minimal O_2 and CO_2 interference if the proper excitation and fluorescence wavelengths are selected. Non-sooting flames with equivalence ratios near one or slightly richer generally exhibit negligible levels of signals from O_2 , and contribution from CO_2 LIF also can be neglected for pressures less than 20 bar. For high-pressure flames (≥ 20 bar) with lean chemistry ($\phi < 0.9$), the interference from CO_2 and O_2 requires more than one detection window for sensitive and accurate detection of NO. In the case of rich flames ($\phi > 1.5$) or flames with incomplete combustion of the fuel, interference from PAH

and other hydrocarbons additionally can complicate NO-LIF measurements and will require further work to establish an appropriate detection strategy.

Accurate 2-D NO-LIF images require corrections for various effects including laser and fluorescence signal attenuation, which vary with gas temperature. For steady laboratory flames, time-consuming strategies such as multi-line NO-LIF fitting [2.2.5] can be used to obtain accurate 2-D temperature fields. For practical applications, 2-line thermometry offers a rapid means to obtain 2-D temperature images with relatively high precision. The temperature fields used in this study are obtained via 2-D 2-line thermometry of NO-LIF (line selection: 226.03 nm and 225.847 nm) and illustrated in Fig. 2.2.2. A detection window centered at 254 nm (FWHM 17.5 nm; Asahi Optics) is used to maximize the signal purity of the NO-LIF.

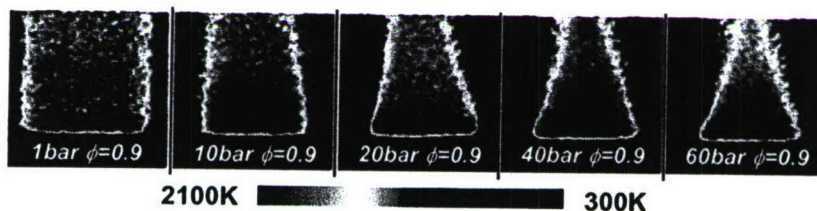


Figure 2.2.2. NO Temperature fields from 2-D 2-line NO-LIF thermometry (line selection : 226.03 nm and 225.847 nm) for various pressures (1–60 bar) at $\phi=0.9$. Obtained by accumulating 20 shots on-chip and using 2-D PLIF imaging of NO-LIF.

Quantitative 2-D NO-LIF images obtained from the multi-window detection strategy are shown in Fig. 2.2.3. The data at pressures of 1 and 10 bar use a two-window (filter 1 & 2) detection, since interference from CO_2 is negligible under these conditions [2.2.4]. The second window provides a means to correct the raw image for the interference of O_2 -LIF in slightly lean conditions ($\phi=0.9$). In slightly rich conditions ($\phi=1.1$), O_2 is mostly consumed during the reaction, and single-window (W1) detection is sufficient (NO-LIF signal selectivity >98%) and no correction is needed. For pressures of 20 bar and higher, a three-window detection strategy is used for correction of the raw images for both O_2 and CO_2 LIF. The additional filters allow simultaneous images of hot CO_2 and O_2 . The data in Fig. 2.2.4 show the image of O_2 and CO_2 extracted from the interference signals for rich and lean 40 bar flames (right side) along with NO images with and without these corrections (left side). It should be noted that the impact of the correction on the NO intensity is not significant due to the fact that the excitation wavelength used already has been optimized for maximum suppression of the interference. The data in Fig. 2.2.3 show that for slightly lean flames ($\phi=0.9$), NO concentrations increase with pressure as predicted by the thermal and prompt NO formation mechanisms. For slightly rich conditions ($\phi=1.1$), NO reburn due to excess hydrocarbons in the flame causes the concentrations to decrease with pressure.

Current Status

Spectrally resolved 1-D line-imaging offers unique advantages in applying single-shot detection of NO-LIF to practical systems. In the current work, 1-D line-imaging measurements are carried out for a range of flame pressures (1–60 bar) and stoichiometries to provide guidelines for filter selection in the multi-window detection strategies used for 2-D measurements. These 1-D measurements do not require the laser

beam to be spread into a sheet, and the higher laser energy intensity results in increased SNR. This work provides practical guidelines for application of instantaneous 1-D or 2-D NO-LIF imaging in high-pressure combustion systems. Further studies to identify the minimum detectable of NO concentrations using 1-D line-imaging are underway.

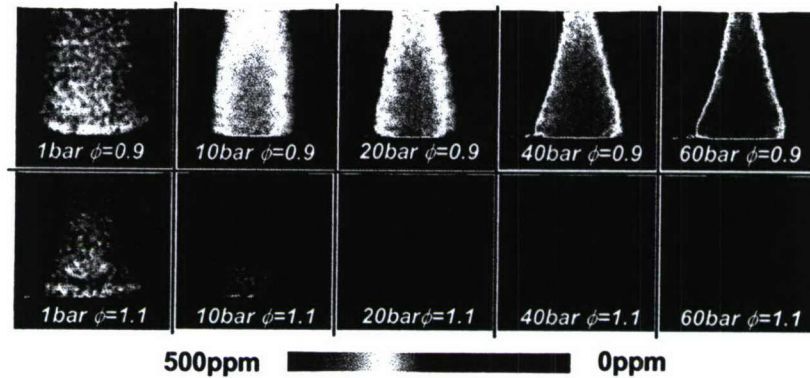


Figure 2.2.3. Quantitative NO concentrations from multi-window 2-D NO-LIF Imaging (1–60 bar, $\phi=0.9$ and 1.1 with 300 ppm NO seeding). Note that the NO concentrations in rich flames are significantly reduced by NO reburn.

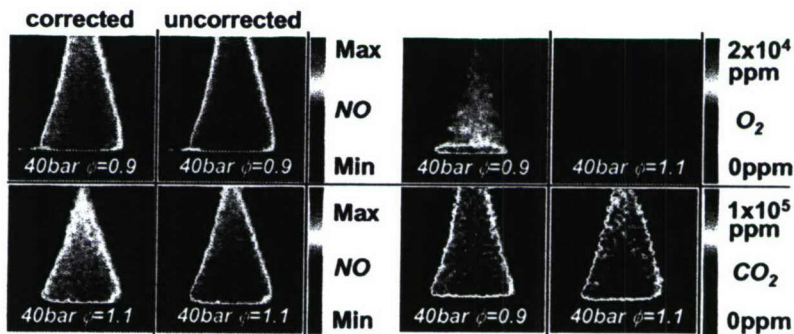


Figure 2.2.4. NO, O₂ and CO₂ concentration fields from a three-window 2-D imaging strategy applied in a 40 bar flame ($\phi=0.9$ and 1.1 with 300 ppm NO seeding). For NO, interference corrected and uncorrected images are both shown (left panel). LIF Intensities are calibrated using Chemkin Premix 1-D flame calculations.

2.2.2 First PLIF imaging of CO₂

UV planar laser-induced fluorescence (PLIF) images of hot carbon dioxide (CO₂) are obtained in a laminar flame (CH₄/air) at high pressure (20 bar) with excitation wavelengths at 239.34 nm and 242.14 nm. Excitation wavelengths are chosen to minimize the contribution of nitric oxide and molecular oxygen LIF signals. Spectrally resolved single-point measurements are used for correction of remaining oxygen LIF interference. The continuum LIF signal from electronically excited CO₂ is detected in a broad (280–400 nm) emission region. The UV PLIF of hot CO₂ has the potential for application to a wide variety of diagnostic needs in high-pressure flames, combustors, and engines.

Background

At room temperature CO₂ is transparent for wavelengths above 200 nm, but recently, with AFOSR support, we discovered that, at flame temperatures, the absorption of hot, vibrationally excited CO₂ extends beyond 300 nm [2.2.3, 2.2.6]. The importance of UV absorption by hot CO₂ for quantitative UV laser diagnostics in combustion systems was recognized only recently [2.2.3]. Subsequently, it was discovered that some of the CO₂ molecules excited by this absorption emit a broadband LIF with a faint, superimposed structure between 200 and 400 nm [2.2.4]. This broadband LIF emission was found to be present in spectrally-resolved measurements in CH₄/air and CH₄/Ar/O₂ flames at elevated pressures, where the intensity of the LIF signal varied with CO₂ absorbance and the lack of signal in a 20 bar H₂/O₂/Ar flame eliminated the possibility of LIF from H₂O. It was shown that the CO₂ signal is linear with number density and laser fluence within the investigated ranges [2.2.4].

During the present AFOSR-grant period, we acquired the first UV LIF images of CO₂ in a laminar, steady high-pressure flame (20 bar). Although these first images are not quantitative concentration maps of CO₂, they illustrate the potential to image the distribution of hot exhaust gases in practical high-pressure combustors.

CO₂ UV Planar Laser Induced Imaging

To image CO₂ in high-pressure flames, a laminar, premixed methane/air flame is stabilized on a porous sintered stainless steel matrix of 8 mm diameter. This facility was developed with AFOSR support and now is used for our measurements of NO-LIF at high-pressure described in section 2.2.1.

Detection of CO₂ in high-pressure flames following absorption of a photon in the 200-300 nm range is complicated by the simultaneous excitation of NO in the A²Σ⁺-X²Π γ bands and O₂ in the B³Σ⁻-X³Σ⁺ Schumann-Runge system. Although pressure broadening increases the overlap in these spectra, an excitation wavelength can be selected that does not overlap with any NO transitions; however, due to the pervasive nature of multiple vibrational bands of O₂ in this region, it is impossible to avoid O₂-LIF interference completely. We choose a strategy to use excitation wavelengths which avoids overlap with NO transitions in the region, while, at the same time, minimizing the overlap with the multiple vibrational bands of O₂. Two candidate excitation wavelengths are selected, 239.34 nm and 242.14 nm, both of which are located between the A-X(0,1) and A-X(0,2) bands of NO, as shown in Fig. 2.2.5. These choices minimize contributions of O₂, as predicted by numerical simulations and confirmed through

experimental excitation scans with wavelength-resolved detection in a lean high-pressure flame ($\phi = 0.8$, $p = 10$ bar), where excess O_2 yields identifiable LIF signal in the burnt gas. In comparison, excitation at 242.14 nm is found to provide the least interference from O_2 with sufficient NO minimization, while 239.34 nm excitation is more selective in completely avoiding any NO transition.

The detection window of the CO_2 -LIF signal extends from 280 to 400 nm. The separation of this spectral region from the laser wavelength ensures suppression of Rayleigh scattering, as well as Raman scattering from other combustion products. The 400 nm blue limit also suppresses background from flame emission, scattered pump-laser, and/or room light. Fig. 2.2.6 shows a spectrally-resolved CO_2 UV-LIF emission spectrum in the center region and outer edge of the flame. The spectral detection window is shown as a box in Fig. 2.2.6. The CO_2 -LIF signal corresponds to the broadband signal evident throughout the entire detection region, although additional emission from O_2 LIF appears as we move towards the outer rim of the flame, where additional air is entrained and O_2 levels are increased.

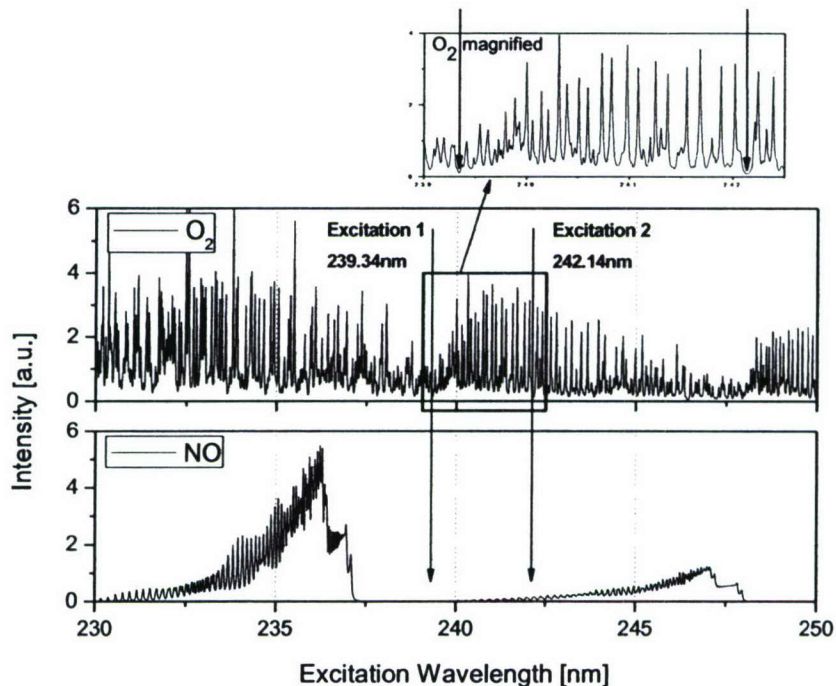


Figure 2.2.5. Simulated LIF excitation spectra of O_2 (upper frame) and NO (lower frame) at 20 bar and 2000 K. A magnified O_2 spectrum near the excitation wavelengths also is shown. 239.34 nm and 242.14 nm excitation lines are shown with arrows.

The resulting images are corrected for laser sheet inhomogeneities and the signal attenuation along the path of the laser beam caused by hot CO_2 and H_2O absorption. Correction of attenuation utilizes recently quantified absorption cross-section data [2.2.3] of hot CO_2 , as well as flame temperatures obtained from multi-line fitting of NO -LIF excitation scans [2.2.7]. Additional correction for O_2 -LIF contribution is carried out by taking spectrally resolved images and extracting spatial distribution of O_2 across the flame and subtracting it from the CO_2 -LIF image. For this, spectrometer measurements are taken at a location 3 mm above the burner matrix using a beam instead of an

expanded laser sheet. The slit of the spectrometer provides the spatial resolution across the horizontal span of the flame. Spatial distribution of CO₂ across the flame can be extracted from the spectrally resolved images by assuming that the signal from the center region of the flame is mainly CO₂. As we move towards the edge of the flame, additional O₂-LIF signal is observed and can be isolated to yield the amount of O₂-LIF interference. The O₂-LIF field is extrapolated to the remainder of the flame using geometrical arguments and assuming uniform composition of the burnt gas.

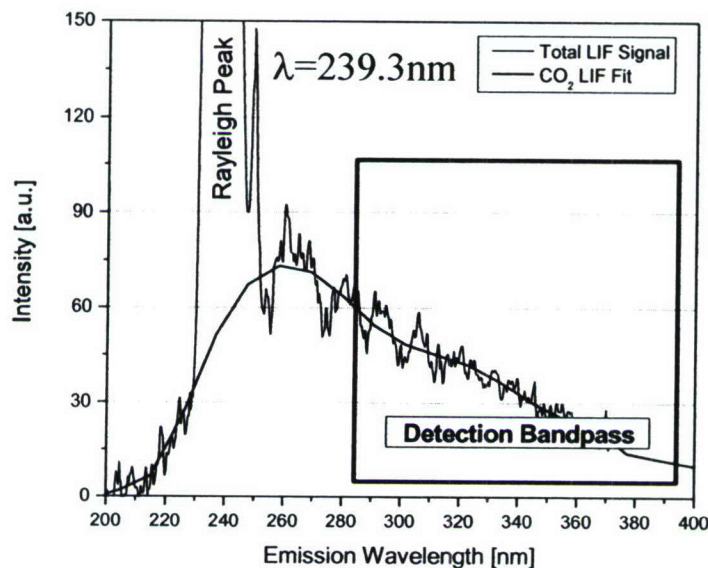


Figure 2.2.6. Spectral detection bandpass (280–400 nm) shown on spectrally-resolved CO₂ UV-LIF spectra with 242.14 nm excitation.

Results

CO₂ visualization using UV-LIF in a 20 bar flame along with signal attenuation along the path of the laser and O₂ contribution information are presented in Fig. 2.2.7. Signal attenuation across the centerline can amount to over 10% at 20 bar across a flame with an exit diameter of 8 mm, as illustrated in image *a* of Fig. 2.2.7 [2.2.3]. Although not required for our small flame, absorption of fluorescence signal also may need to be considered as it radiates from the plane of the excitation light sheet to the collecting lens. The attenuation correction requires knowledge of the temperature field, which is determined for this flame using a multi-line NO-LIF temperature imaging technique [2.2.5]. For the work reported here, attenuation corrections are made for the excitation laser beam using Beer-Lambert's law with absorption cross-section data. A pixel by pixel attenuation correction across the centerline of the flame is made, and image *a* of Fig. 2.2.7 shows the magnitude of attenuation calculations.

Image *b* is the interference O₂-LIF for excitation at 239.34 nm, and data for 242.14 nm excitation are similar. The observed O₂-LIF contribution in the stable center region of the flame is around 1% of the entire LIF signal for our flame conditions (equivalence ratio of $\phi = 1.1$), which we attribute to noise in the extraction process. The O₂

concentration increases around the edges of the flame, where air from the secondary flow is entrained into the system.

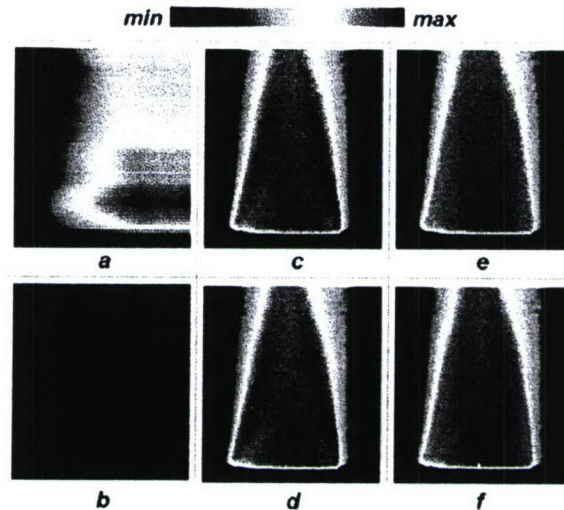


Figure 2.2.7. Results of imaging analysis of CO₂ UV-PLIF **a** total attenuation due to hot CO₂ and H₂O (239.34 nm excitation); **b** O₂-LIF contribution; **c** and **d** CO₂-LIF and O₂-LIF combined image for 239.34 nm and 242.14 nm excitation, respectively; **e** and **f** final CO₂-LIF image for 239.34 nm and 242.14 nm excitation, respectively with O₂-LIF correction. Images **b–f** share same scale and image **a** is ten times more sensitive.

Images *e* and *f* of Fig. 2.2.7 show the final CO₂-LIF distribution using UV LIF with excitation at 239.34 nm and 242.14 nm, respectively. CO₂-LIF intensities remain fairly constant to a first-order estimate throughout the hot burnt gas region. Previous studies with spectrally resolved point measurements show that the relative contribution of CO₂-LIF signals increases with pressure and can become a significant interference source in the detection of other minor species in post combustion gases.

Current Status

We present 2D-LIF images of hot CO₂ using UV excitation in the burnt gases of a premixed, high-pressure laminar flame. To our knowledge, these are the first CO₂ images published using UV-excitation and detection. Excitation at 239.34 nm and 242.14 nm effectively can avoid overlap with NO transitions in the region and minimizes any overlap with the multiple vibrational bands of O₂. A first-order correction for residual interference from O₂ LIF has been performed by using spectrally resolved emission measurements of the flame. Further understanding of spectral features exhibited by CO₂ will be required to enable a more detailed and quantified isolation of the O₂ contribution.

The CO₂ excitation is strongly temperature-dependent, and this visualization strategy will isolate the high temperature regions of the combustion effluent, possibly proving a measurement strategy to infer temperature in flames with uniform CO₂ concentrations. The strategy reported here for UV visualization of high-temperature CO₂ in high-pressure combustion exhaust also may prove very useful to understand mixing phenomena in a variety of practical combustion devices.

Further work is planned to image CO₂ at higher-pressures (~60 bar) and to quantify the temperature and wavelength-dependence of the CO₂ fluorescence quantum yield. Correction methods utilized in the current study are limited to stable flames, and additional investigation into single-shot measurement techniques will also be addressed.

High-Pressure LIF References

- [2.2.1] M. D. DiRosa, K. G. Klavuhn, R. K. Hanson, "LIF spectroscopy of NO and O₂ in high-pressure flames," *Combustion Science and Technology* **118** (1996) 257-283.
- [2.2.2] W. G. Bessler, C. Schulz, T. Lee, J. B. Jeffries, R. K. Hanson, "Strategies for laser-induced fluorescence detection of nitric oxide in high-pressure flames: I. A-X (0,0) excitation," *Applied Optics* **41** (2002) 3547-3557; "Strategies for Laser-Induced Fluorescence Detection of Nitric Oxide in High-Pressure Flames: II. A-X (0,1) Excitation," *Applied Optics* **42** (2003) 2031-2042; "Strategies for Laser-Induced Fluorescence Detection of Nitric Oxide in High-Pressure Flames: III. Comparison of A-X Detection Schemes," *Applied Optics* **42** (2003) 4922-4936.
- [2.2.3] C. Schulz, J. B. Jeffries, D. F. Davidson, J. D. Koch, J. Wolfrum, R. K. Hanson, "Impact of UV absorption by CO₂ and H₂O on NO LIF in high-pressure combustion applications," *Proceedings of the Combustion Institute* **29** (2002) 2735-2742.
- [2.2.4] W. G. Bessler, C. Schulz, T. Lee, J. B. Jeffries, R. K. Hanson, "Carbon dioxide UV laser-induced fluorescence in high-pressure flames," *Chemical Physics Letters* **375** (2003) 344-349.
- [2.2.5] T. Lee, W. G. Bessler, H. Kronmayer, C. Schulz, J. B. Jeffries, "Quantitative temperature measurements in high-pressure flames with multi-line NO-LIF thermometry," *Applied Optics* **44** (2005) 6718-6728.
- [2.2.6] C. Schulz, J. D. Koch, D. F. Davidson, J. B. Jeffries, R. K. Hanson, "Ultraviolet absorption spectra of shock-heated carbon dioxide and water between 900 and 3050 K," *Chemical Physics Letters* **355**, 82-88 (2002).
- [2.2.7] W. G. Bessler, C. Schulz, T. Lee, D.-I. Shin, M. Hofmann, J. B. Jeffries, J. Wolfrum, R. K. Hanson, "Quantitative NO-LIF imaging in high-pressure flames," *Applied Physics B* **75** (2002) 97-201.

2.3. Temperature diagnostics based on CO₂ absorption of UV light

A diagnostic for microsecond-time-resolved temperature measurements using ultraviolet laser absorption of vibrationally hot CO₂ is developed. The absorption ratio of continuous wave laser radiation near 244 and 266 nm is used to determine temperature. Precise temperature-dependent absorption cross sections are measured for CO₂ at the two laser wavelengths. Measurements behind shock waves in both non-reacting and reacting (ignition) systems are made and comparisons to isentropic and constant volume calculations are performed to validate the temperature measurement technique.

Background

At room temperature CO₂ is transparent at wavelengths longer than 205 nm, but at high temperature (>1000 K) CO₂ has significant absorption in the 190-310 nm spectral range due to vibrationally excited molecules. With AFOSR support, we have investigated the feasibility of a thermometry technique using the strongly temperature-dependent CO₂ absorption cross-section in this region [2.3.1]. We first measured the ultraviolet absorption cross-section of CO₂ in the wavelength region 216.5-306 nm [2.3.2]. The spectrally smooth nature of the absorption and its strong temperature-dependence suggest the use of two-wavelength absorption-based thermometry for high-temperature gases where CO₂ is present. Additionally, the absorption cross-section shows no pressure dependence in experiments up to 8 atm, and none is expected at higher pressures due to its smooth pre-dissociative nature, enabling high-pressure temperature measurements.

The CO₂ absorption cross-section $\sigma(\lambda, T)$ is independent of pressure in the wavelength range of interest and can be described using a semi-empirical form

$$\ln \sigma(\lambda, T) = a + b\lambda \quad (2.3.1)$$

where $a = c_1 + c_2T + c_3/T$ and $b = d_1 + d_2T + d_3/T$. The CO₂ cross-section, $\sigma(\lambda, T)$, is in units of $10^{-19} \text{ cm}^2 \text{ molecule}^{-1}$, the wavelength, λ , is in units of 100 nm, and the temperature, T , is given in units of 1000 K. The following parameters from Oehlschlaeger et al.[2.3.2] provide a best fit to the absorption cross-section measurements: $c_1 = 0.05449$, $c_2 = 0.13766$, $c_3 = 23.529$, $d_1 = 1.991$, $d_2 = -0.17125$, and $d_3 = -14.694$. This fit can be used over the range of the cross-section measurements: 1500-4500 K and 216.5-306 nm.

Taking the ratio of absorbance at two different laser wavelengths gives

$$\frac{\text{absorbance}(\lambda_1)}{\text{absorbance}(\lambda_2)} = \frac{\sigma(\lambda_1, T)n_{\text{CO}_2}L}{\sigma(\lambda_2, T)n_{\text{CO}_2}L} = \frac{\sigma(\lambda_1, T)}{\sigma(\lambda_2, T)} = R(T) \quad (2.3.2)$$

allowing the measurement of temperature independent of knowledge of CO₂ concentration or path length. For the measurements presented here we chose to use cw-laser radiation at 244 and 266 nm. These two wavelengths can be generated conveniently and simultaneously with available laser sources, avoid most major interference absorption, and have an appropriate wavelength separation for measurement of temperature in the region of interest in shock wave experiments and combustion studies. A polynomial expression for temperature as a function of the absorbance ratio (cross-section ratio) from 1500-4500 K is given by

$$T = (2.857 \times 10^4)R^4 - (3.043 \times 10^4)R^3 + (1.478 \times 10^4)R^2 + (9.57 \times 10^2)R + 1041 \text{ [K]} \quad (2.3.3)$$

where R is the ratio of 266 to 244 nm absorbance ($R = \text{absorbance}(266 \text{ nm}) / \text{absorbance}(244 \text{ nm})$).

The CO_2 absorption cross-section at 244 and 266 nm is plotted versus temperature in Fig. 2.3.1. The uncertainty in temperature measurements made using the absorbance ratio method is limited by the magnitude of the fractional absorption, particularly at the more weakly absorbing wavelength 266 nm. The measured ratio has greater uncertainty at low temperature due to smaller absorbance (lower SNR); therefore, the inferred temperature is more uncertain at lower temperatures. An uncertainty in absorbance due to SNR limitations of $\pm 0.1\%$ ($-\ln(I/I_0) = \pm 0.001$) generally is achievable in shock wave experiments regardless of the magnitude of the absorbance. The uncertainty in measured temperature is mapped as a function of temperature and the product of partial CO_2 pressure and path length ($P_{\text{CO}_2}L$) in Fig. 2.3.2. The uncertainty decreases at higher temperature and pressure. The uncertainties given in Fig. 2.3.2 assume an uncertainty of $\pm 0.1\%$ in absorbance ($-\ln(I/I_0) = \pm 0.001$), and the contours represent the percentage uncertainty in the measured temperature. The favorable uncertainty contours in Fig. 2.3.2 demonstrate the attractiveness of this diagnostic for high-pressure, high-temperature measurements.

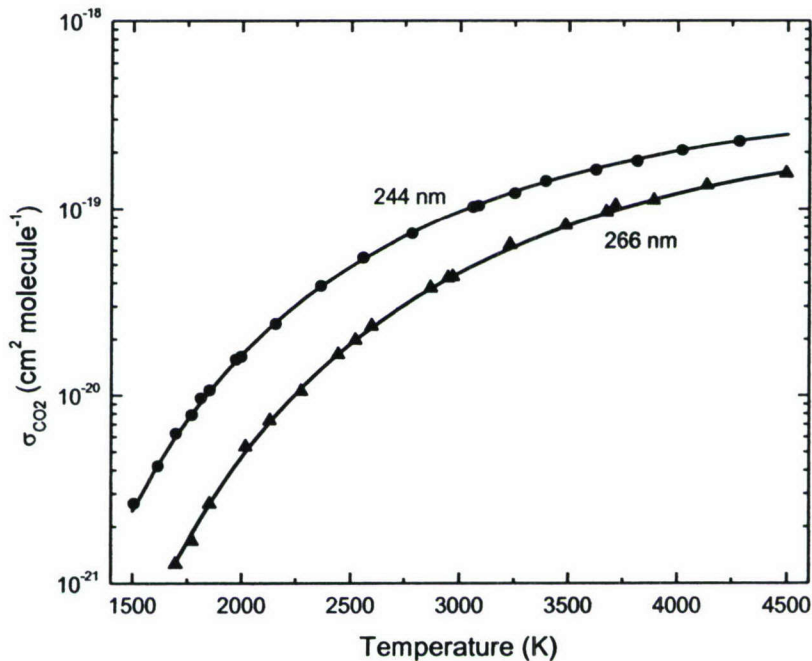


Figure 2.3.1. Measured CO_2 absorption cross-section at 244 and 266 nm.

Demonstration of Time-Resolved Temperature Measurements

The technique to measure time-resolved temperature using the ratio of CO_2 absorption at two UV wavelengths is demonstrated behind reflected shock waves in a pressure-driven (helium), high-purity stainless steel shock tube, as illustrated in Fig. 2.3.3. The incident and reflected shock conditions are calculated using the ideal normal shock equations. Uncertainties in the experimental pressure and temperature given by the shock equations are $<1\%$ in the CO_2/Ar mixtures and $<2\%$ in the $\text{CH}_4/\text{O}_2/\text{CO}_2/\text{Ar}$

Broca prisms. The two UV laser beams (1.5 mW each) each are split into two components: one component, less than 1 mm in diameter, passing through the shock tube windows (UV fused silica) at a location 2 cm from the endwall, and one detected prior to absorption as a reference. The beams are detected using amplified S1722-02 Hamamatsu silicon photodiodes (risetime < 1.0 μ s, 4.1 mm diameter) and recorded on a digital oscilloscope.

Experiments are performed with several test gas mixtures to demonstrate the diagnostic and to characterize the effect of energy release behind shock waves. Experiments first are performed in test mixtures of 5 and 10% CO₂ dilute in argon. Finally, experiments are performed in several stoichiometric mixtures of CH₄/O₂/CO₂/Ar to demonstrate the diagnostic in experiments with varying levels of energy release due to chemical reactions.

An example non-reacting experiment is shown in Fig. 2.3.4 for a 10% CO₂/Ar test mixture (all data are filtered to 1 MHz time resolution). The temperature is inferred with the 266/244 absorbance ratio method described above and is found to be nearly constant for 2 ms before several abrupt changes produced by gas dynamics. These changes are due to interaction of the reflected shock wave with the contact surface (helium/test gas interface) and interaction of the reflected shock wave with the rarefaction wave (expansion of helium driver gas). Additionally, a comparison of the measured temperature is made with the temperature calculated from the pressure trace via the assumption of an isentropic relationship between pressure and temperature

$$T = T_0 \left(\frac{P}{P_0} \right)^{\frac{\gamma-1}{\gamma}} \quad (2.3.5)$$

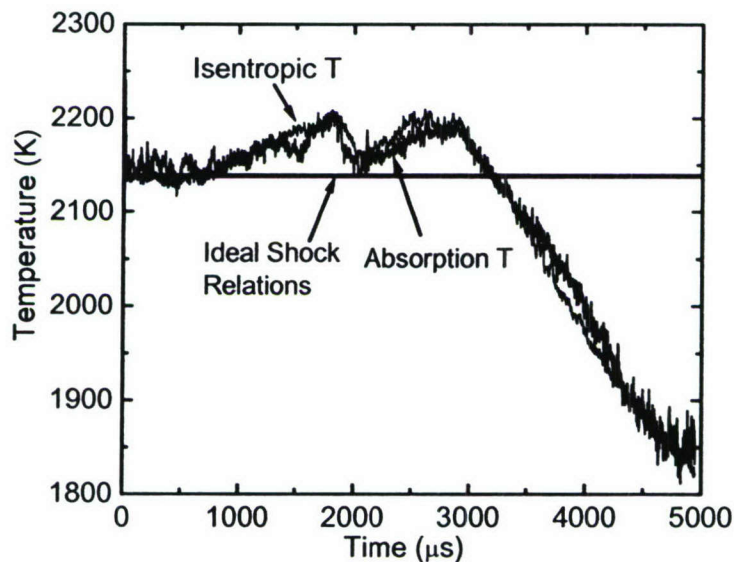


Figure 2.3.4. Example non-reacting experiment: with initial reflected shock conditions from ideal shock relations: 10% CO₂/Ar, 2138 K and 0.121 MPa. Measured temperature (dark line) vs isentropic temperature (light line), measured temperature determined from absorbance ratio, and isentropic temperature determined from pressure measurement.

A comparison of the temperature measured using the absorbance-ratio method with that resulting from the isentropic assumption shows excellent agreement (Fig. 2.3.4), with a difference in the two of no greater than 2% for this experiment. This good agreement serves both to validate the CO₂ temperature sensor and to confirm that for shock wave experiments with no energy release the isentropic assumption holds.

Forty-two experiments are conducted over a wide range of temperature and CO₂ concentration. The scatter in the difference between the measured temperature and the ideal temperature has a 1- σ standard deviation of 0.6% and is no greater than 2.3%. The CO₂ absorbance at 266 and 244 nm ranges from 0.5 to 13% and 2 to 32%, respectively, illustrating the large dynamic range of conditions investigated.

To demonstrate the CO₂ absorption technique for thermometry in combustion systems and to characterize the effects of energy release on temperature in shock tube studies, we perform a set of ignition experiments in CH₄/O₂/CO₂/Ar mixtures; the time-resolved temperature is shown in Fig. 2.3.5. Three mixtures are used: (1) 1% CH₄/ 2% O₂/ 10% CO₂/ dilute in argon, (2) 2% CH₄/ 4% O₂/ 10% CO₂/ dilute in argon, and (3) 4% CH₄/ 8% O₂/ 10% CO₂/ dilute in argon.

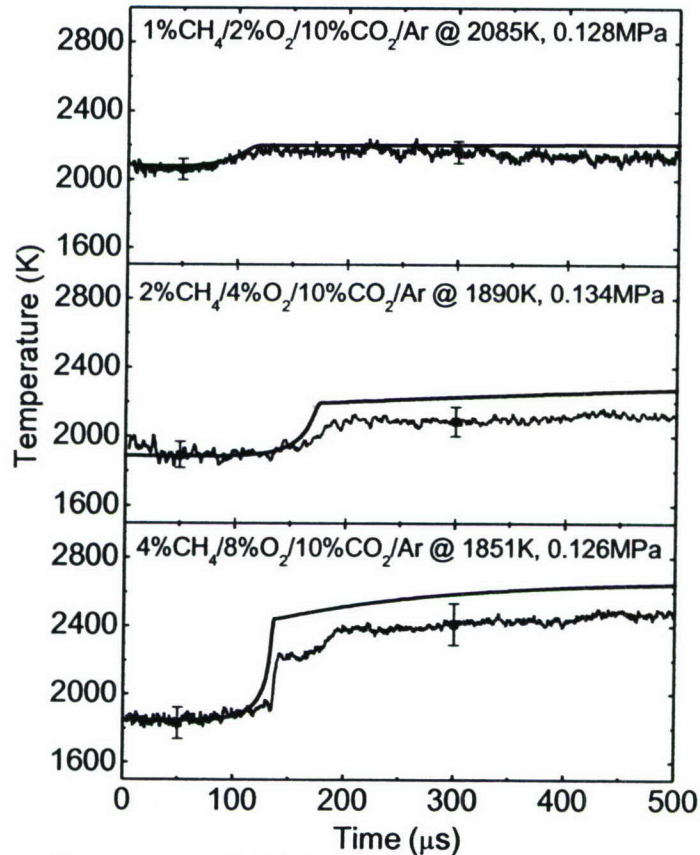


Figure 2.3.5. Measured temperature (solid thick lines) versus constant volume calculation (solid thin lines). Top graph (initial reflected shock conditions): 1% CH₄/ 2% O₂/ 10% CO₂/ Ar, 2085 K, and 0.128 MPa. Middle graph: 2% CH₄/ 4% O₂/ 10% CO₂/ Ar, 1890 K, 0.134 MPa. Bottom graph: 4% CH₄/ 8% O₂/ 10% CO₂/ Ar, 1851 K, 0.126 MPa. Post-shock vibrational equilibrium is assumed. Error bars represent a 1- σ confidence interval.

These CO₂ combustion measurements required experiments to investigate potential interference absorption from hot CH₄ and O₂. Absorption by CH₄ at these wavelengths is undetectable, but absorption by hot O₂ is detectable and requires a small correction to the measurements at 244.061 nm. A chemical model and the estimated gas temperature are sufficient to determine the small correction of the absorption by O₂ at 244.061 nm. This interference can be avoided with a different UV cw laser source that can be tuned in wavelength to an O₂ absorption minimum. Simulations of the O₂ spectrum at 2000 K and 0.1 MPa in this wavelength range find that the interference could be reduced by a factor of seven by tuning between two absorption lines to a value near 243.99 nm.

The resulting temperature time histories are given in Fig. 2.3.5 for the three combusting gas mixtures along with comparison to model results calculated using a constant volume constraint and the GRI 3.0 methane combustion mechanism. A comparison between constant volume model calculations and measured temperature shows good agreement for the ignition delay and the overall trends in temperature; however, the post-ignition temperature plateau measured with laser absorption is lower, in all three cases than that predicted with the constant-volume model. This shortcoming of the constant volume model is expected because as energy is released due to ignition and the test gas temperature begins to rise at the test section location (2 cm from endwall) the hot combustion gases will expand down the shock tube, resulting in a somewhat lower temperature plateau. (The measured lower temperature in the post-ignition plateau is accounted for when determining the O₂ interference absorption cross-section at 244 nm.) For the examples given in Fig. 2.3.5 the measured post-ignition temperature rise is 60-75% of that predicted by the constant volume model.

Current Status

We currently are working to modify the constant volume model and have found good success using the CHEMKIN package coupled with the measured pressure history. Initial experiments have yielded excellent agreement with measured temperature time-histories. We believe that this development of a CHEMKIN solver for reactive flows behind reflected shock waves is a significant development that will increase substantially the utility of shock tubes for studying combustion chemistry.

UV CO₂ Absorption Temperature References

- [2.3.2] M. A. Oehlschlaeger, D. F. Davidson, J. B. Jeffries, R. K. Hanson, "Ultraviolet absorption cross-sections of hot carbon dioxide," *Chemical Physics Letters*. **399** (2004) 490-495.
- [2.3.1] J. B. Jeffries, C. Schulz, D. W. Mattison, M. A. Oehlschlaeger, W. G. Bessler, T. Lee, D. F. Davidson, R. K. Hanson, "UV absorption of CO₂ for temperature diagnostics of hydrocarbon combustion applications," *Proceedings of the Combustion Institute* **30** (2005) 1591-1599.

2.4 Advanced wavelength-multiplexed diode laser absorption diagnostics

Results from three different diode laser absorption sensor strategies are highlighted. First, we investigate the use of multiple absorption transitions with different temperature dependence to unravel non-uniform temperature dependence. The development of an absorption sensing strategy for non-uniform temperature distributions along the line-of-sight (LOS) may increase the potential applications of this already successful sensing strategy. Second, we show the improved SNR for absorption sensing in the model scramjet facility at Wright Patterson Air Force Base using a scanned wavelength-modulation spectroscopy (WMS) strategy. The results show the importance of careful optical design engineering and illustrate the potential of this sensing strategy for routine use in hypersonic ground test. Third, we discuss recent fuel-sensing results using a novel mid-IR laser source based on difference frequency generation (DFG). This new laser and our differential absorption strategy have the potential for sensitive detection of a wide variety of hydrocarbon fuels.

2.4.1. Non-uniform temperature distributions

Two measurement strategies to determine non-uniform temperature distributions in combustion gases using line-of-sight (LOS) absorption spectroscopy have been examined in detail. These strategies rely on measurements of multiple absorption transitions of a single species, each with unique temperature dependence. The first strategy, called profile fitting, mathematically fits the observed absorption measurements constrained with a postulated temperature distribution. The second strategy, called temperature binning, determines the temperature probability density function (PDF) along the LOS using prescribed temperature bins. The wavelength-multiplexed (WM) sensor concepts and the mathematical representations are first explored by simulation calculations. Then these concepts are demonstrated in a laboratory arrangement with two distinct temperature regions. The measured “2-Zone” T/X_{H_2O} distribution is composed of a hot flame zone ($T \approx 1500$ K, $X_{H_2O} \approx 10\%$) and a cold room-air zone ($T \approx 300$ K, $X_{H_2O} \approx 2\%$) each with the same pathlength. The experimental results demonstrate that a non-uniform temperature distribution can be characterized with either strategy. The measurement accuracy will increase with the number of transitions and also with the use of optimally chosen transitions. The experimental results also confirm that use of known physical constraints to reduce the number of degrees of freedom improves the interpretation of the measurement results and thus the sensor performance.

Background

Laser absorption spectroscopy has become a successful sensor strategy for fast, non-intrusive, sensitive, and reliable *in situ* measurements of multiple flow field parameters such as temperature, pressure, velocity, and species concentration in a variety of practical combustion and propulsion flows [2.4.1]; however, this line-of-sight (LOS) sensing technique traditionally has been limited to flow fields with nearly uniform properties. In practical flow fields, significant temperature and species concentration gradients may exist along the measurement path for optical diagnostics due to flow mixing, chemical reaction, phase change, heat transfer with the side walls, and other effects. Tomographic reconstruction of laser absorption along multiple lines-of-sight has been demonstrated in

laboratory experiments to resolve these non-uniformities, but practical systems seldom have sufficient optical access and the sensor redundancy necessary for quantitative application of tomographic techniques.

Extension of LOS absorption measurements to non-uniform flow fields has been explored previously, including work to correct for boundary layer effects, to reduce sensitivities to flow non-uniformities, and to correlate pattern factors with the path-averaged temperatures inferred from different line pairs. Current efforts build on our earlier AFOSR-sponsored work that first demonstrated the potential to extract the temperature distribution information from simultaneous measurements of multiple absorption transitions [2.4.2]. Our current work uses simulation calculations to investigate systematically the two strategies: (1) profile fitting and (2) temperature binning. Then a demonstration experiment is performed using a wavelength-multiplexed sensor with an optical path length that has two distinct temperature regions (~1500K and ~300K). This experiment exploits a Zolo fiber-coupled multiplexer to combine five laser beams onto a single beam path and a Zolo fiber-coupled de-multiplexer to disperse the collected transmitted light onto five separate detectors. These five lasers interrogate seven absorption transitions, which are used to investigate a “2-Zone” temperature/mole-fraction distribution. These results demonstrate the sensor concept and provide a preliminary investigation of sensor performance.

Theoretical Principles

Building on the ideas first demonstrated in our previous AFOSR-sponsored work, we first assume that m (>2) transitions have been selected and their integrated Beer’s Law absorbances, A_i , have been determined from the WM-LOS absorption measurements. We use these simulated data to compare the results from the profile-fitting and temperature-binning strategies.

Principles of Profile Fitting

The profile-fitting strategy first requires a postulated distribution of temperature along the measurement path to constrain the temperature profile fitting. For example, in a confined combustion flow, the gas temperature often has a cold boundary layer, and the simplest representation would be a “2-T” profile with a core flow at an average temperature of T_c and a boundary layer with an average temperature of T_b and a thickness of L_b , as shown in panel **a** of Fig. 2.4.1. A more complex, but common, representation would be a parabolic profile constrained by the center temperature of T_c and the wall temperature of T_w , as shown by panel **b**. Another somewhat more sophisticated model would be a uniform core flow at a temperature of T_c and a boundary layer with parabolic temperature distribution constrained by the wall temperature of T_w and the boundary layer thickness of L_b , as shown in panel **c**. These postulated temperature distribution profiles can be represented by a general functional form as follows

$$T(x) = f(T_{char}, L_{Tchar}, x), \quad (2.4.1)$$

where T_{char} is the characteristic temperature such as T_c , T_w and T_b , and L_{Tchar} is the characteristic length such as L_b . Similarly, the shape for the absorber mole fraction distribution also is postulated using physical constraints

$$X_{abs}(x) = g(X_{char}, L_{Xchar}, x), \quad (2.4.2)$$

where X_{char} is the characteristic mole fraction and L_{Xchar} the corresponding length.

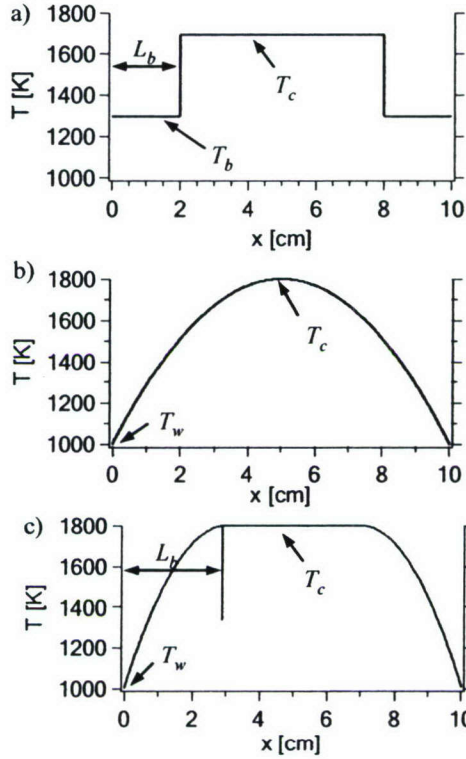


Figure 2.4.1. Postulated temperature distribution profiles for confined combustion gases with cold walls.

Based on the presumed temperature and mole fraction profiles, the integrated absorbance of any transition can be calculated. For the selected m transitions, a nonlinear equation set can be established

$$\begin{cases} A_1 = P \int_0^L g(X_{char}, L_{Xchar}, x) \cdot S_1(f(T_{char}, L_{Tchar}, x)) dx \\ A_2 = P \int_0^L g(X_{char}, L_{Xchar}, x) \cdot S_2(f(T_{char}, L_{Tchar}, x)) dx \\ \vdots \\ A_m = P \int_0^L g(X_{char}, L_{Xchar}, x) \cdot S_m(f(T_{char}, L_{Tchar}, x)) dx \end{cases} \quad (2.4.3)$$

Once the number of equations, i.e. the number of measured absorption transitions m , is larger than the number of unknowns, Eqn. set (2.4.3) can be solved by nonlinear least-square fitting

$$\min_{T_{char}, L_{Tchar}, X_{char}, L_{Xchar}} \sum_{i=1}^m \left(P \int_0^L g(X_{char}, L_{Xchar}, x) \cdot S_i(f(T_{char}, L_{Tchar}, x)) dx - A_i \right)^2 \quad (2.4.4)$$

to obtain the set of T_{char} , L_{Tchar} , X_{char} and L_{Xchar} that best describe the postulated temperature and mole fraction profiles.

Expression 2.4.4 presents the most general mathematical model for the profile-fitting strategy. It can be simplified by using more physical constraints. For example, if the temperature non-uniformity in a combustion flow results mainly from the non-uniform local equivalence ratio, the mole fraction distribution of the absorber, e.g. water vapor, can be assumed to be similar to the temperature distribution, i.e.

$$g(X_{char}, L_{char}, x) = c \cdot f(T_{char}, L_{Tchar}, x) \quad (2.4.5)$$

where c is a constant to be inferred from the fitting along with T_{char} and L_{Tchar} . When such a relationship is utilized in the profile fitting, the number of unknowns will be reduced significantly. As another example, the mole fraction can be assumed to be constant along the measurement path in cases where the temperature non-uniformity is much more significant than that of the mole fraction. Finally, measurements by other sensors, CFD calculations, past knowledge on the target flow field or a similar system, etc., can be used to constrain some of the variables and reduce the number of unknowns in the postulated temperature profile. For example, thermocouples can be used to measure the gas temperature near the wall, T_w , so that this quantity is known.

The profile-fitting strategy obviously requires using physical understanding of the flow fields to constrain the temperature and mole fraction distributions along the measurement path. Simulation studies have demonstrated that the measurement results will be improved significantly by using as many physical constraints as possible to reduce the number of unknowns in the postulated temperature profile.

Principles of Temperature Binning

If *a priori* knowledge of the flow fields is not readily accessible, the temperature-binning method can be utilized to extract the characteristic information on the LOS non-uniformities. The temperature-binning method is also useful for cases where the temperature distribution of the flow fields cannot be represented by a simple profile or cases where obtaining an exact temperature distribution profile is not necessary for the application. The temperature-binning method is derived from a discretization of the path integral of the absorbance

$$\tilde{A} = \frac{A}{P} = \sum_{j=1}^n (S(T_j) \cdot X_{abs,j} \cdot L_j), \quad (2.4.6)$$

which implies decomposing the entire measurement path with non-uniform properties into n sections, each with a nearly uniform temperature of T_j , absorber mole fraction of $X_{abs,j}$ and path length of L_j . For the selected m absorption transitions, the following linear equation set can be established:

$$\begin{bmatrix} S_1(T_1) & S_1(T_2) & \cdots & S_1(T_n) \\ S_2(T_1) & S_2(T_2) & \cdots & S_2(T_n) \\ \vdots & \vdots & \vdots & \vdots \\ \vdots & \vdots & \vdots & \vdots \\ S_m(T_1) & S_m(T_2) & \cdots & S_m(T_n) \end{bmatrix} \cdot \begin{bmatrix} (X_{abs}L)_1 \\ (X_{abs}L)_2 \\ \vdots \\ (X_{abs}L)_n \end{bmatrix} = \begin{bmatrix} \tilde{A}_1 \\ \tilde{A}_2 \\ \vdots \\ \tilde{A}_m \end{bmatrix}, \quad (2.4.7)$$

where the n temperature bins are prescribed based on a rough estimation of the possible temperature range along the measurement path. Once the number of absorption transitions is larger than the number of temperature bins, i.e. $m > n$, The set of equations 2.4.7 can be solved by constrained linear least-square fitting

$$\min_{(X_{abs}L)_j} \sum_{i=1}^m \left(\sum_{j=1}^n (S_i(T_j) \cdot (X_{abs}L)_j) - \tilde{A}_i \right)^2, \quad (2.4.8)$$

such that $(X_{abs}L)_j \geq 0$ ($j = 1, \dots, n$).

The solution for $(X_{abs}L)_j$, called column density, is actually the probability density function (PDF) of the absorbing species. More physically meaningful results can be inferred from the PDF solution if other physical constraints are available. For example, if the mole fraction of the absorbing species can be assumed to be constant, the fraction of path length (f_j) for each temperature bin can be calculated from the column density since

$$f_j = \frac{(X_{abs}L)_j}{\sum_{j=1}^n ((X_{abs}L)_j)} = \frac{L_j}{L}. \quad (2.4.9)$$

Figure 2.4.2 shows such a case, where the combustion gas temperature along the measurement path has a parabolic distribution, as plotted in panel **a**, and the mole fraction of absorber can be assumed to be constant. Ten temperature bins within a typical combustion temperature range of 1000-2000 K have been prescribed. Panel **b** shows the exact PDF solution, which reveals that no temperature is higher than 1800 K along the measurement path since the two highest-temperature bins are empty and $\sim 35\%$ of the entire path is at the temperature of 1700-1800 K, while only 6% is at 1000-1100 K, etc. This example illustrates that non-intrusive and rapid measurements of this type can be useful in characterizing channel flows, e.g., in connection with process control.

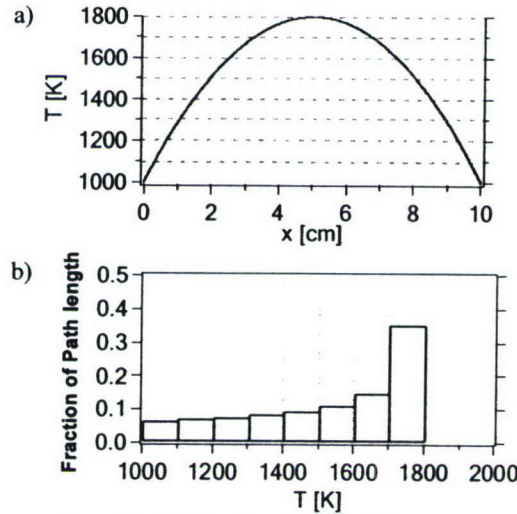


Figure 2.4.2. Parabolic temperature distribution (panel a) and the temperature-binning result for this distribution (panel b).

Simulation studies have shown that increasing the number of bins n (for fixed number of transitions m) will deteriorate the measurement accuracy. Thus, a moderate number of bins, e.g. five, should be used initially and more bins justified only if more transitions can be measured. In spite of the limited number of bins and the lack of information on the spatial arrangement of the bins along the path, the PDF solution is sufficient for many monitoring and control applications where the goal focuses on minimizing or maximizing the non-uniformities, e.g. pattern factor sensing and control, or on monitoring the fluctuations in the PDF solution in studies of turbulence.

Demonstration Experiments

The two strategies to interpret LOS absorption measurements in flows with a non-uniform temperature distribution are demonstrated by laboratory measurements of a “2-Zone” temperature distribution with a wavelength-multiplexing (WM) scheme. H₂O vapor is selected as the absorbing species because it is naturally present in the atmosphere, it is a major product of hydrocarbon combustion, and it has strong rovibrational overtone transitions in the near-infrared that overlap with readily available telecommunication diode lasers.

A “2-zone” temperature LOS experiment is conducted to illustrate the measurement and data analysis concepts. The schematic of the experiment is shown in Fig. 2.4.3. The free space laser beam has a total path length of 54 cm set by the spacing between the pitch lens and the catch lens. A 25.4 cm long flat-flame burner is located at the center of the measurement path to create a uniform hot section. Therefore, the entire LOS

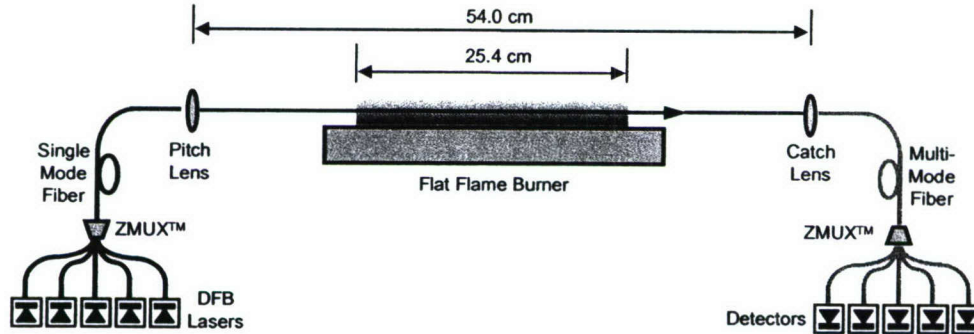


Figure 2.4.3. Schematic of the experimental setup for a five laser multiplexed absorption sensor.

measurement path can be divided roughly into two zones, one in the cold room air and the other in the hot flame gases. This experimental arrangement is illustrative of combustion flows with confined flames that do not fill the flame chamber or duct completely. The flat flame burner is fueled by premixed ethylene and dry air, and a stable laminar flame can be obtained over the equivalence ratio range of 0.6-1.4. For the current demonstration experiments, the ethylene and air flow rates are measured to be 1.8 slm (standard liters per minute) and 34.0 slm, respectively, by calibrated rotameters. The equivalence ratio is thus 0.76, which leads to an equilibrium water vapor mole fraction of 0.1 with an uncertainty of ± 0.03 due to the measurement uncertainty of the fuel/air flow rates.

The flame temperature is measured at the height of the laser beam (5 mm above the burner surface) by a type S thermocouple with a bead size of 2 mil (51 μm), and radiation corrections of 55 K are applied. The core part of the flame (1-24 cm) has a uniform temperature distribution. The average is 1534 K, with an uncertainty of 3% estimated from the scatter of the thermocouple readings and the uncertainty in the radiation correction. This measured flame temperature is lower than the adiabatic flame temperature at the measured equivalence ratio mainly due to the radiation loss to the surroundings and the heat conduction to the water-cooled burner surface. At both edges of the flame, there is a very slight temperature rise and then a sharp drop to the room temperature, thus creating well-defined high- and low-temperature zones along the LOS measurement path.

The thermocouple measurement of the room temperature is 298 K, which agrees with the readings of a mercury thermometer. The room air humidity is measured by a calibrated hygrometer to be 56%, which indicates a water mole fraction of 1.75%.

Wavelength-Multiplexed Diode Laser Absorption Measurements

The layout of the WM scheme also is shown in Fig. 2.4.3. The fiber-coupled outputs from five distributed-feedback (DFB) lasers are combined and coupled into one single-mode fiber by a multiplexer (Zolo Technologies). The multiplexed laser beam is collimated by the pitch lens and propagates across the “2-Zone” measurement path. Another lens is used to catch the free space laser beam and focus it into a multi-mode fiber that leads to a grating-based demultiplexer (Zolo Technologies). The wavelength-multiplexed beam then is diffracted into the constituent five wavelengths, collected on fiber for each channel and delivered to five InGaAs detectors.

The five DFB lasers emit near 1343, 1345, 1392, 1395 and 1398 nm. The fiber-coupled, echelle grating based ZMUXTM multi/demultiplexers are chosen over free space, conventionally ruled gratings because these compact devices allow dense wavelength multiplexing and demultiplexing (up to 44 wavelengths) with high efficiency, pre-set alignment, and well-controlled polarization-dependent loss and thermal drift.

The DFB lasers can be scanned across 2-3 cm^{-1} by injection current variation, enabling access to the seven strong water vapor transitions listed in Table 1. These seven transitions are used for this experiment to illustrate the proposed sensor concepts and demonstrate the feasibility, though they are not the optimum choice for the current temperature range. All five lasers are scanned simultaneously at 1 kHz with a linear current ramp. The transmitted laser signals obtained by the five detectors are recorded simultaneously at a 5 MHz sampling rate.

Data Reduction

The recorded raw-data scans from each of the five channels are corrected for detector DC off-sets and background emission, although most of the emission from the flame has been rejected by the ZMUXTM demultiplexer, which acts as a band-pass filter with a narrow bandwidth of ~ 1 nm for each channel. The corrected raw data for each channel then are averaged for every ten sequential scans to reduce stochastic noise. The resulting time response of this demonstration measurement is 10ms, owing to the ten sweep average of the 1 kHz wavelength scans. (This time response is not a maximum for the technique, as we have routinely made scanned-wavelength direct absorption measurements at 10kHz and have performed limited demonstration measurements at

scan rates of 50 kHz .) From each averaged laser scan (i.e. the transmitted signal I_t), the unattenuated laser intensity (i.e. the baseline I_0) is determined by fitting the part of the I_t trace without absorption with a polynomial.

Table 1 Spectroscopic parameters of the seven water vapor transitions used in the demonstration experiments.

Line Index	ν_0 [cm ⁻¹]	$S(T_0)$ [cm ⁻² atm ⁻¹]	E'' [cm ⁻¹]
1	7154.35	3.670E-04	1789.04
2	7164.90	3.550E-03	1394.81
3	7185.60	1.960E-02	1045.06
4	7417.82	1.070E-02	1079.08
5	7444.36	1.100E-03	1786.00
6	7164.07	2.021E-02	300.36
7	7419.17	2.222E-02	842.36

The integrated absorbances A_i for the seven lines are calculated from the measured absorption spectra. The data reduction is more complicated than that for uniform cases since the lineshape measured along a non-uniform temperature distribution no longer can be modeled by a single Voigt function. Once the integrated absorbances for the seven lines are obtained, either the profile-fitting strategy or the temperature-binning strategy can be applied to characterize the non-uniform temperature distribution using the models above. The spectroscopic parameters of the seven transitions used in the calculations are listed in Table 1.

If we assume that both the temperature and water mole fraction along the LOS measurement path are uniform, this “uniform” temperature can be inferred from the ratio of measured absorbance of any line pair. Here line pair 1 and 2 yields 1199 K, while line pair 1 and 3 produces 1122 K. This discrepancy suggests non-negligible non-uniformities, thus illustrating the value of the new strategy to use multiple absorption measurements to characterize the actual temperature distribution.

Profile-Fitting Results

In the profile-fitting calculation, the shape of the non-uniform property distribution must be postulated in advance. The layout of the experimental setup (hot flame temperature in the middle with cold room temperatures on both sides) enables us to postulate a “2-Zone” profile, as shown in Fig. 2.4.4, to model the temperature and mole fraction distribution along the LOS measurement path. The unknowns (free parameters) to be solved from the multiple absorption measurements are the temperature and mole fraction for each zone, i.e. T_1 , T_2 , X_1 and X_2 . We investigate four different interpretations of the measured absorption data, each with a different number of constraints on the postulated distributions. For each of these four cases, the influence of the number of lines on the sensor performance is investigated.

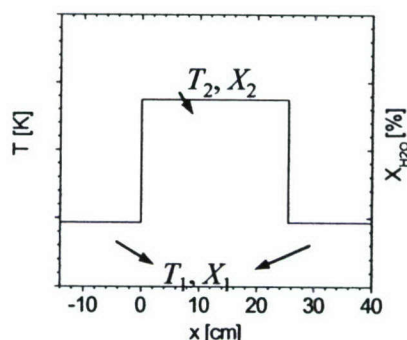


Figure 2.4.4. The “2-Zone” property distribution postulated for profile-fitting calculation.

In case 1, the measured absorbances are fit with all four unknowns T_1 , T_2 , X_1 and X_2 as free parameters, and the average values are listed in Table 2. Both the measurement accuracy, as indicated by the difference between the measured and the expected values,

Table 2 The average values of the profile-fitting results (and percentage deviation from the expected values) with different number of lines for cases 1 and 2.

Lines	Case 1				Case 2		
	T_1 [K]	T_2 [K]	X_1 [%]	X_2 [%]	T_1 [K]	T_2 [K]	X_2 [%]
1-5	309	1374	1.1	8.4	227	1264	7.8
	(4%)	(-10%)	(-37%)	(-16%)	(-24%)	(-18%)	(-22%)
1-7	292	1489	1.7	9.4	295	1524	9.7
	(-2%)	(-3%)	(-3%)	(-6%)	(-1%)	(-1%)	(-3%)
Expected	298	1534	1.75	10.0	298	1534	10.0

and the statistical precision, increase appreciably with the addition of data from lines 6 and 7. By using the absorbances measured on lines 1-5, the temperature and mole-fraction inferred deviate significantly from the expected values, which is due partly to the narrow span of the lower state energy E'' of these 5 transitions. By adding measurements from line 6 and 7 with much lower E'' , the results for T_1 , T_2 , X_1 and X_2 quickly converge to the expected values within an accuracy of 2%, 3%, 3% and 6% respectively. This result illustrates the importance of optimized selection of absorption transitions.

In case 2, the H_2O mole fraction of the cold zone X_1 is fixed at 1.75%, which is determined using the measured humidity and an estimated temperature (300 K) of the room air. The three remaining unknowns T_1 , T_2 , and X_2 then are allowed to vary in the nonlinear least square fit, and the average values are listed in Table 2. Again the measurement accuracy increases systematically with the addition of data from lines 6 and 7. By using all 7 transitions, the T_1 , T_2 , and X_2 can be measured within an accuracy of 1%, 1%, and 3%, respectively, which improves from the corresponding results for case 1.

Generally speaking, the addition of physical constraint(s) improves the accuracies of the fit values.

In case 3, the H₂O mole fractions for the two zones X_1 and X_2 are fixed at 1.75% and 10% (the equilibrium value for the measured equivalence ratio), respectively. Since there are only two remaining unknowns, T_1 and T_2 , a minimum number of 3 lines is required for the nonlinear least squares fit, and the average values are listed in Table 3. These fit results reveal the same trend, namely an increasing of the accuracy of the fit values with an increased number of lines. Even with the minimum number of lines, however, satisfactory results of T_1 and T_2 can be obtained (with an accuracy of 4% and 1%, respectively) by fixing the H₂O mole fraction values.

Table 3 The average values of the profile-fitting results (and percentage deviation from the expected values) with different number of lines for cases 3 and 4.

Lines	Case 3		Case 4	
	T_1 [K]	T_2 [K]	T_2 [K]	X_2 [%]
1-3	286 (-4%)	1516 (-1%)	1487 (-3%)	9.4 (-6%)
1-5	302 (1%)	1554 (1%)	1520 (-1%)	9.6 (-4%)
1-7	299 (0%)	1552 (1%)	1537 (0%)	9.8 (-2%)
Expected	298	1534	1534	10.0

In case 4, the properties of the room air T_1 and X_1 are fixed in the fit, and thus only the properties of the hot flame zone T_2 and X_2 are the free parameters, and the average values are listed in Table 3. The accuracy increases with the number of lines, particularly with the inclusion of lines 6 and 7. Using all 7 transitions, T_2 and X_2 are determined within an accuracy of 1% and 2%, respectively.

This two-zone measurement arrangement clearly is applicable to cases with interference absorption by humid room air bounding a relatively uniform hot zone of interest. Only the temperature and water content of the hot target gas typically are desired, but sometimes room air inevitably is enclosed in the LOS beam path near the pitch or catch optics, since the laser sources or the measurement geometries prohibit using fibers to deliver the laser beam directly to the edge of the flow fields to be measured. Normally, in our laboratory, the open path in this boundary is purged with N₂ to remove the interference absorption by the room air, but the purging efficiency cannot be guaranteed for all applications, especially if the purging system is not well-designed, installed, and maintained. By using more than two transitions, as is done in case 4, the flow field properties of interest can be inferred directly from the LOS absorption data without installing complex purging systems.

Table 4 shows a comparison of the profile-fitting results for all four cases when data from all 7 transitions are used. It confirms that the fitting results improve significantly when the number of unknowns (free parameters) in the postulated distribution profiles can be reduced by using physical constraints.

Temperature-Binning Results

Alternatively, we can interpret the absorption data using the temperature-binning strategy. An estimation of the possible temperature range along the LOS measurement path allows the prescription of five temperature bins as shown in Fig. 2.4.5. All seven

Table 4 Comparison of the profile-fitting results (and percentage deviation from the expected values) for all four cases with all 7 lines.

Case	T_1 [K]	T_2 [K]	X_1 [%]	X_2 [%]
1	292 (-2%)	1489 (-3%)	1.7 (-3%)	9.4 (-6%)
2	295 (-1%)	1524 (-1%)	--	9.7 (-3%)
3	299 (0%)	1552 (1%)	--	--
4	--	1537 (0%)	--	9.8 (-2%)
Expected	298	1534	1.75	10.0

transitions are used in the analysis. The resultant column densities ($X_{\text{H}_2\text{O}}L$)_{*j*}, as represented by the solid bars, are very close to the expected PDF solutions, as indicated by the dash-dot lines. Only the two side bins have non-zero solutions. They suggest that the LOS measurement path can be modeled approximately as two zones, one at ~300 K and the other at ~1500 K, which are very close to the conditions of the experiment. The population of water vapor in the highest temperature bin is much larger than that in the lowest temperature bin, which implies that the “2-T” distribution might result from a cold spot somewhere along an otherwise uniform high temperature region or a cold boundary layer on both sides of a uniform hot core temperature. Up to this point, no *a priori* knowledge of the flow fields, except for an estimate of the possible temperature range, has been applied to extract the characteristic information on the LOS non-uniformities discussed above.

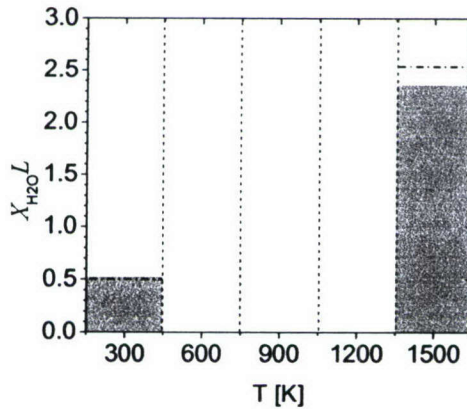


Figure 2.4.5. Illustration of the temperature-binning results solved using all 7 transitions with five bins.

Current Status

We have performed an initial laboratory demonstration of two strategies for measurements of non-uniform temperature distributions using line-of-sight (LOS) absorption spectroscopy. Based on the measurements of multiple absorption transitions with different temperature dependences, the profile-fitting strategy fits a postulated temperature distribution profile, while the temperature-binning strategy determines the temperature probability density function (PDF) along the LOS using prescribed

temperature bins. Both strategies can be modeled mathematically as least-square fitting problems. In the non-optimized demonstration experiment, a “2-Zone” temperature/mole-fraction distribution created in laboratory is measured with a wavelength-multiplexing scheme where five DFB diode lasers are multiplexed to probe seven absorption transitions of water vapor. The absorption data are analyzed by both strategies to illustrate the sensor concepts and investigate the sensor performance. The experimental results demonstrate that a non-uniform temperature distribution can be characterized with either strategy by measuring the LOS absorption for a limited number of transitions with different temperature dependences. The measurement accuracies will increase with the number of transitions and with the use of optimally chosen transitions. Use of known physical constraints also provides important value in properly interpreting measurement results and improving the sensor performance. Further work is planned to develop design rules for the selection of absorption transitions. Using an optimized set of absorption transitions, the next step envisioned includes demonstration experiments in systems with realistic temperature profiles.

2.4.2. Scanned-wavelength-modulation for high SNR absorption

A wavelength-multiplexed diode laser absorption sensor is developed and tested for the measurement of gas temperature and the concentration of water vapor in a model scramjet combustor in Test Cell 22 of the Air Force Research Laboratory (AFRL) Propulsion Directorate at Wright-Patterson AFB. This sensor uses multiple diode lasers to monitor beam steering and three spectral features of water vapor in the near infrared region. The measurements are made near the exit of the scramjet combustor. An important aspect of the work is the optical engineering used to overcome beam steering from the high-speed flow and fiber-mode-noise. Test measurements at AFRL are made with the sensor using two detection strategies: (1) scanned-wavelength direct absorption and scanned-wavelength-modulation spectroscopy (scanned-WMS) with second harmonic detection ($2f$), and the noise performance of the two sensor architectures are compared. The WMS- $2f$ technique produces superior noise rejection and improved overall signal to noise ratios compared to direct absorption.

Background

Traditionally, scanned-wavelength direct absorption spectroscopy has been the technique of choice for aero-engine applications because of its simplicity, accuracy, and ability to make absolute measurements [2.4.1]. In harsh combustion environments such as the scramjet, however, the technique can suffer from low signal-to-noise ratios arising from mechanical and gasdynamic beam steering, weak absorption at high temperatures, and fiber mode noise. The scanned-direct absorption technique must rely entirely on careful optical engineering to reduce noise to acceptable levels. Another technique that has been explored for its increased sensitivity to small signals and ability to reject noise is wavelength modulation spectroscopy (WMS) with second harmonic detection ($2f$). This technique, often simply referred to as WMS- $2f$, employs a lock-in amplifier to isolate the second harmonic of the detected signal, greatly enhancing the noise rejection characteristics. Example signal-to-noise ratio (SNR), temperature, and fast-Fourier transform (FFT) data obtained in a scramjet combustor using both scanned-direct absorption and WMS- $2f$ under nearly identical operating conditions will be compared to illustrate the benefits of WMS- $2f$ in harsh environments.

Sensor Architecture and Experimental Design

The sensor utilizes a beam of infrared light consisting of the multiplexed output of four TDLs. The light is pitched across the combustor exit plane, collected, and dispersed onto four separate detectors. Three of the lasers are wavelength-scanned across H_2O transitions and used to infer the static temperature via direct absorption and WMS- $2f$. The fourth laser is fixed at a non-resonant wavelength to detect transmission perturbations from gasdynamic or mechanical beam steering, window fouling, or particulates in the flow.

A schematic of the optical arrangement of the sensor is shown in Fig. 2.4.6. Four fiber-coupled DFB diode lasers are multiplexed with a 9-micron single-mode fiber combiner. A 10-meter single-mode fiber delivers the beam to the scramjet test section, where it is pitched across the combustor exit with an aspheric collimating lens. After traversing the test region, the beam is collected with a large diameter lens and focused into a 400 micron multimode fiber. The beam travels through the multimode fiber to a

demultiplexing setup a few meters from the test section. The light exits the multimode fiber and is collimated by a large diameter aspheric lens onto a 30 mm square, 1200 grooves/mm diffraction grating. The dispersed light beams are focused onto separate 3mm diameter InGaAs photodetectors.

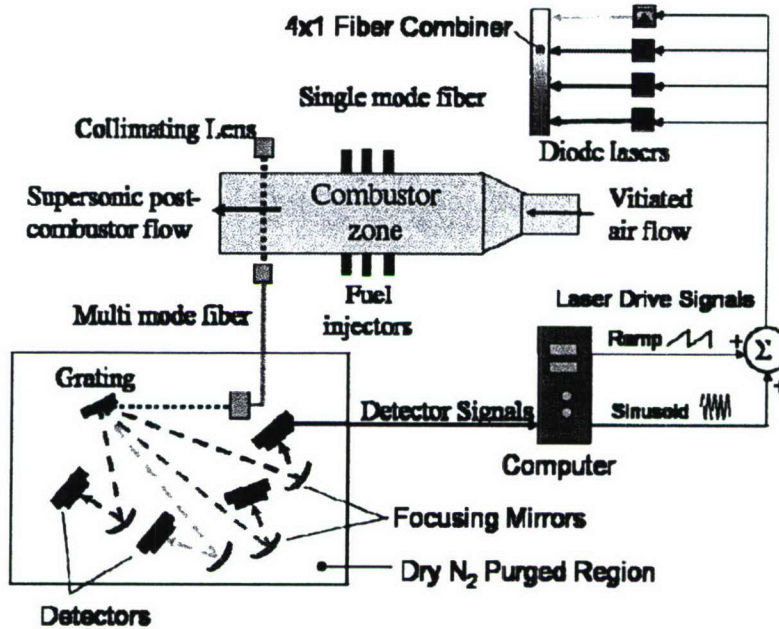


Figure 2.4.6. Schematic of optical setup.

The scramjet test facility at Wright-Patterson Air Force Base in Dayton, Ohio will not be covered in detail here because an in-depth treatment is available in the literature[2.4.3]. Compressed air (up to 13.6 kg/s and 920K) is vitiated to raise the pre-expansion temperature. Make-up oxygen replaces that burned in the vitiator heater. The gas stream is expanded to supersonic speeds through a Mach 2.7 nozzle. Liquid JP-7 fuel is heated to a vaporized condition and injected to the near atmospheric pressure gases just upstream of a cavity-based flameholder.

The combustor is fitted with 2.5 cm x 12 cm quartz optical access ports located 16.5 cm upstream of the end of the combustor. The outward face of each window is wedged to avoid optical interference effects that arise when scanning laser wavelength in the presence of parallel optical faces in the beam path. The collimating pitch and catch optics are arranged on translation stages that can traverse the optical ports vertically while maintaining beam alignment.

All absorption spectroscopy techniques rely on careful selection of the quantum transitions (lines) that will be used to probe the gaseous flow. Careful selection begins by choosing transitions of a species present in the flow (in this case, water vapor) with desirable absorption properties for the particular application. For these experiments, three lines are chosen with different lower state energies. The lower state energy, determines the equilibrium molecular population in the absorbing state as a function of temperature and thus can be used to describe how the absorption strength of a particular transition varies with temperature. The three transitions used for these experiments are shown in Table 2.4.5. The lower state energies are chosen to give peak temperature

sensitivity for the 1392 nm and 1343 nm features at 500 K and the 1392 and 1469 nm features at 1600 K. These temperatures coincide with the expected temperature of a scramjet run with only the vitiator operating and with full combustion, respectively.

The three lines also are chosen for their isolation from other transitions, laser availability, and correct wavelength spacing to allow dispersal by the grating. The key spectral parameter of line strength is validated for each feature under carefully controlled conditions in a laboratory furnace.

Table 2.4.5. Line strength and lower state energy parameters for spectroscopic features used in these experiments.

Wavelength nm (Hitran '04)	Frequency cm^{-1} (Hitran '04)	Line Strength (296 K) $cm^{-2} atm^{-1}$ (Hitran '04)	Line Strength (296 K) $cm^{-2} atm^{-1}$ (Measured)	Lower State Energy cm^{-1} (Hitran '04)
1392	7185.6	$1.97(10)^{-2}$	$1.96(10)^{-2}$	1045.1
1343	7444.35 and 7444.37	$1.12(10)^{-3}$	$1.10(10)^{-3}$	1774.8 and 1806.7
1469	6807.83	$1.02(10)^{-6}$	$6.48(10)^{-7}$	3319.4

Measurement Techniques: Scanned-Wavelength Direct Absorption

Scanned-wavelength direct absorption has been a staple of TDL sensors for harsh environments. The important aspects of the technique are shown in Fig. 2.4.7. The injection current of the TDL is driven with a linear ramp signal (in this case, a 4 kHz

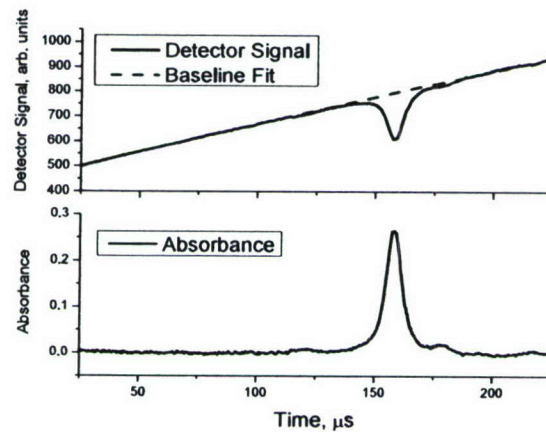


Figure 2.4.7. (top) Raw detector signal during a full combustion run for a single direct absorption laser scan with baseline fit (1392 nm feature); (bottom) Absorbance plot resulting from laser scan and baseline.

sawtooth signal). The linear ramp in injection current produces a near-linear variation in laser intensity that can be seen in the top panel. The variation in laser intensity is accompanied by a near-linear change in laser wavelength. As the laser is tuned across the absorption feature some light is absorbed, reducing the detector signal. A baseline fit is performed on the non-absorbing “wings” of the feature to infer the laser intensity in the absence of absorption. The Beer-Lambert relation (Eqn. 2.4.10) can be rearranged to yield Eqn. 2.4.11, which gives the absorbance (α) as a function of the transmitted laser intensity (I_t , the detector signal), and the incident laser intensity (I_o , the baseline fit). The absorbance plot resulting from the laser scan is shown in the lower panel.

$$\frac{I_t}{I_o} = \exp(-\alpha) \quad (2.4.10)$$

$$\alpha = -\ln\left(\frac{I_t}{I_o}\right) \quad (2.4.11)$$

The absorbance is a function of line strength (S), species partial pressure (P_i), pathlength (L), and line shape function (ϕ), as shown in Eqn. 2.4.12.

$$\alpha = S(T) \times P_i \times L \times \phi(\nu) \quad (2.4.12)$$

The line shape is a normalized function that describes the profile of a spectroscopic transition in frequency space. Thus if the measured absorbance of a transition is fit with the proper profile (a Voigt profile is used here) and integrated with respect to frequency, the line shape function is equal to unity and is no longer important. This step is shown in Eqn. 2.4.13, where the result from integrating with respect to frequency is called the integrated absorbance area.

$$area = S(T) \times P_i \times L \times \int_{-\infty}^{\infty} \phi(\nu) \cdot d\nu = S(T) \times P_i \times L \quad (2.4.13)$$

For thermometry, the ratio of the integrated area of two absorption features is used. When the ratio is calculated, the species partial pressure and pathlength cancel. The remaining ratio of line strengths is purely a function of temperature and is used to infer the temperature from the measured area ratio.

$$\frac{area_1}{area_2} = \frac{S_1(T)}{S_2(T)} \quad (2.4.14)$$

The species concentration is calculated using Eqn. 2.4.13 with one spectral feature. The area and pathlength are known, and the line strength is calculated using the temperature previously inferred from the ratio.

Measurement Techniques: Scanned-WMS-2f

The theory of WMS with 2f detection has been covered extensively in the literature [2.4.4]. It is used generally in situations involving small absorbances and/or noisy environments. In its most basic form, WMS-2f involves rapidly modulating the laser wavelength, passing the light through an absorbing medium, and running the detector signal through a lock-in amplifier set to isolate the signal at twice the modulation frequency. The resulting signal can be used to calculate various gasdynamic properties. In the scanned-wavelength variant of WMS-2f employed here, the rapidly modulated laser wavelength also is tuned slowly across an absorption feature, and the peak height of the WMS-2f signal is used to infer gas properties. The top panel of Fig. 2.4.8 depicts the raw detector signal of a single sweep of scanned-WMS-2f. As with the direct absorption method discussed before, the laser injection current is driven with a linear ramp (2 kHz), but now there is also a high frequency sinusoid superimposed on the ramp (190 kHz). The laser intensity varies with the drive signal and is accompanied by a similar variation in laser wavelength.

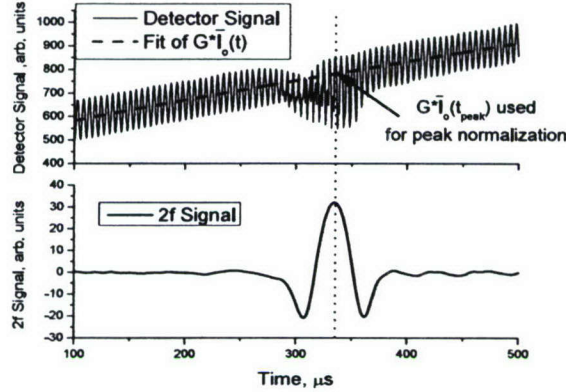


Figure 2.4.8. (top) Raw detector signal during a full combustion run for a single laser scan with modulation (1392 nm feature). Also shown is fit to obtain $G \cdot \bar{I}_o(t)$. (bottom) WMS- $2f$ signal resulting from laser scan.

The laser frequency (inverse wavelength), $\nu(t)$, and the laser intensity, $I_o(t)$, for the situation described above are given by Eqn. 2.4.15 and 2.4.16.

$$\nu(t) = \bar{\nu}(t) + a \cos(\omega t) \quad (2.4.15)$$

$$I_o(t) = \bar{I}_o(t) [1 + i_o(t) \cos(\omega t + \psi)] \quad (2.4.16)$$

where $\bar{\nu}(t)$ and $\bar{I}_o(t)$ are the average laser frequency and intensity that are varying slowly due to the linear ramp, ω is the modulation frequency, a is the frequency modulation amplitude, and $i_o(t)$ is the intensity modulation amplitude (that is a constant normalized by $\bar{I}_o(t)$). ψ is the phase shift between frequency and intensity and is commonly assumed in the literature to be π radians. Due to the small modulation depths utilized for this work, this assumption is made with minimal resulting error; however real diode lasers have a value of ψ that is somewhat greater than π and can be measured to investigate the magnitude of this simplification.

When modulated laser light at a frequency corresponding to a quantum transition is passed through an absorbing medium, it is attenuated. The intensity of light that remains after having passed through the medium (I_t) is proportional to a transmission coefficient (τ) that is a function of the frequency of the light:

$$I_t(t) = I_o(t) \cdot \tau(\bar{\nu} + a \cos \omega t) \quad (2.4.17)$$

Because the transmission coefficient is a periodic, even function in ωt , it can be expanded in a Fourier cosine series. The mathematical details will not be shown here, but the resulting signal, normalized by the average laser intensity and detector gain ($G \bar{I}_o$), is given by Eqn. 2.4.18. This equation assumes linear frequency and intensity modulation with a phase shift of π . Equation 2.4.18 could be written as a function of time because the average laser frequency varies in time with the linear ramp of injection current. It will be advantageous to express the WMS- $2f$ signal in terms of average laser frequency for the purpose of comparing with simulations.

$$\frac{S_{2f}(\bar{\nu})}{G\bar{I}_o(\bar{\nu})} = \frac{1}{2} \left[H_2 + \frac{i_o(\bar{\nu})}{2} (H_1 + H_3) \right] \quad (2.4.18)$$

When taking the ratio of WMS-2f peak height signals from two spectral lines the partial pressure and pathlength cancel, leaving only the line shape integral and line strength for each line. Fortunately, the modulation depth of each laser can be chosen such that the line shape integral is nearly constant for moderate changes in pressure and mixture composition. This important point is discussed in detail by Liu *et al.* [2.4.5]. Thus, if WMS-2f peak height simulations are performed at the nominal expected partial pressure for both lines as a function of temperature, the resulting ratio of the two simulations will form a map between WMS-2f peak ratio and temperature. This map will be unaffected by moderate changes of mixture composition and pressure about the nominal value used for simulation.

To infer gas properties, the measured signals are compared with simulations. For temperature, the measured WMS-2f peak ratio is compared with the map described above. To calculate partial pressure of the species, the simulation for one spectral line (at the temperature inferred by the two line ratio) is ratioed with the measured peak height of that line. The WMS-2f signal is directly proportional to the partial pressure of the species, so the ratio of the measured WMS-2f signal and the simulation will exactly equal the ratio of the measured partial pressure and the partial pressure used in simulation.

$$\frac{\left(\frac{S_{2f}(\bar{\nu}_{peak})}{G\bar{I}_o(\bar{\nu}_{peak})} \right)_{measured}}{\left(\frac{S_{2f}(\bar{\nu}_{peak})}{G\bar{I}_o(\bar{\nu}_{peak})} \right)_{simulated}} \cdot P_{H_2O,simulated} = P_{H_2O,measured} \quad (2.4.19)$$

The method above yields absolute measurements of temperature and concentration so long as rough values of pressure and mole fraction are known. Thus, careful normalization of the WMS-2f peak height and the use of full simulations with judiciously chosen and measured laser parameters (a , i_o), enables quantitative measurements without the traditional WMS-2f calibration.

The scanned-wavelength direct absorption method works well in environments where spectrally-isolated features with large absorbances can be used and noise eliminated with optical engineering. However, as is the case with scramjets and other applications to harsh flows, some level of noise always will be present, and high temperatures will require the use of weakly absorbing features. WMS-2f offers certain advantages that can address these issues.

Baseline fitting is a key component of scanned-wavelength direct absorption data reduction; however, several factors increase the difficulty of making a good fit. Fiber mode noise causes time and wavelength-dependent fluctuations that bend and distort the intensity ramp of the detector signal. Gasdynamic and mechanical beam steering causes signal fluctuations, resulting in further errors. In the limit that optical engineering can

control the aforementioned noise sources, a difficulty that is still present is interference from neighboring spectral features. Determining where baseline fits should begin and end to avoid the wings of the main and neighboring spectral features greatly complicates baseline fitting. This effect is apparent in Fig. 2.4.7 and especially is evident for the 1343 and 1469 nm features in Fig. 2.4.9.

For small modulation depths, the WMS- $2f$ signal in the absence of absorption is zero regardless of laser intensity. The WMS- $2f$ signal thus rides on a zero background and does not depend on any baseline fitting. The measured WMS- $2f$ peak height must be normalized by $G\bar{I}_0$ in order to compare with the simulations. A low-order polynomial is fit through the high frequency modulation to perform the normalization, as shown in the top panel of Fig. 2.4.8. While it may seem that an error in the fit through the WMS- $2f$ signal would induce the same problems as an error in the baseline fit of a direct absorption scan, there is a difference of relative measurement scales that reduces the relative contribution to the signal uncertainty. As an example, a 1% error in the fit of $G\bar{I}_0$ used to normalize the WMS- $2f$ signal will result in only a 1% error in the normalized WMS- $2f$ peak height. However, since the absorbance is measured relative to the

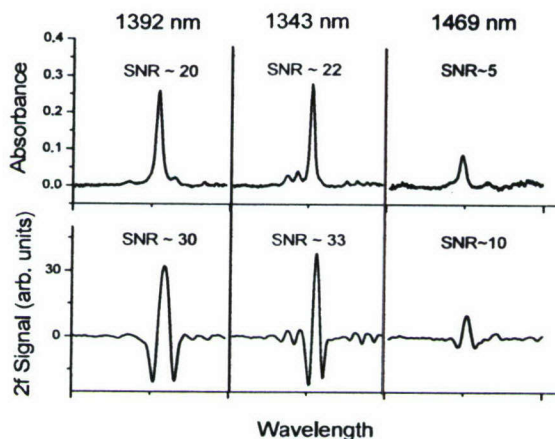


Figure 2.4.9. Comparison of direct absorption and WMS- $2f$ signals during a full combustion run.

baseline fit of a direct absorption scan, a 1% error on the baseline fit for a transition with 10% peak absorbance will cause a 10% error; whereas a 1% error in the estimate of I_0 for WMS- $2f$ produces a 1% error in the signal. For this reason WMS- $2f$ is less prone to baseline fitting errors than direct absorption.

With direct absorption spectroscopy one must rely entirely on optical engineering to reduce noise. WMS- $2f$, however, employs the use of a lock-in amplifier that serves to shift the detection bandwidth above most noise sources. The lock-in amplifier multiplies the detector signal by a sinusoidal reference wave at twice the modulation frequency. The components of the detector signal thus are shifted in frequency space such that the signal at twice the modulation frequency becomes a DC signal. This signal then is filtered low-pass to eliminate the shifted signals outside the low pass filter cutoff, thereby eliminating nearly all but the signal at twice the modulation frequency. For the experiments presented here, the modulation frequency is 190 kHz. The lock-in amplifier multiplies the detector signal by a 380 kHz sine wave and then low-pass filters the result

with a 75 kHz cutoff, 8th order IIR cascade filter. The resulting signal thus only contains signals that are originally at 380 kHz +/- 75 kHz. Because most noise sources are below 300 kHz (including 1/f laser noise), they are filtered out and do not contribute to the final signal.

Comparison of Direct Absorption and WMS-2f Results

Results of gas temperature and H₂O concentration are obtained in the scramjet on consecutive runs with the same combustor conditions to compare direct absorption and WMS-2f. Figure 2.4.9 shows an example scan for each line obtained during a full combustion run with both methods. The top panel shows absorbance data that come from fitting a baseline to the raw laser scan. The neighboring features reduce the percentage of each scan that can be fit with the critical zero absorbance baseline. Also, the features overlap, complicating Voigt fitting and the determination of the integrated absorbance area. The bottom panel shows the WMS-2f data under the same scramjet conditions. The neighboring features appear as perturbations next to the main feature (that are not factored into the SNR). These features do not affect the measurement of the peak height because the zero baseline of the WMS-2f signal is inherent and does not arise from a baseline fit. The contribution of the neighboring features to the WMS-2f peak height is small and accounted for by the simulations. Comparison of the SNR for each feature shows the improvements possible with WMS-2f. The SNR for the high temperature 1469 nm feature is improved by a factor of two.

Figure 2.4.10 shows a comparison of the measured temperatures using the 1392/1469 nm line pair with direct absorption and WMS-2f. The WMS-2f data have a 2 kHz sampling rate (1 WMS-2f peak per laser scan at 2 kHz), so the direct absorption data are filtered to 2 kHz from their original 4 kHz sampling rate to give a fair comparison. The figure shows an improvement in the standard deviation of the temperature fluctuations from 90 K to 50 K.

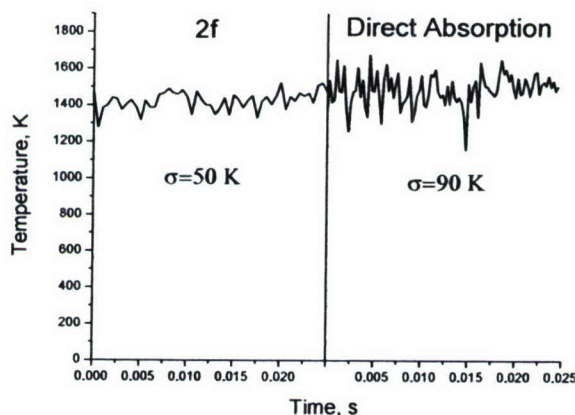


Figure 2.4.10. Comparison of measured temperature using direct absorption and WMS-2f with the 1392/1469 nm line pair. The direct absorption data is filtered from 4 kHz to 2 kHz to match the WMS-2f sampling rate. $\phi = 1.02$.

Figure 2.4.11 shows 0.75 seconds of representative temperature and H₂O partial pressure data. A portion of the start-up transient of the scramjet combustor is shown. The mean temperature increases for approximately 0.45 seconds before stabilizing, while

the mean H_2O partial pressure remains stable throughout. These data can be used to characterize transients in the scramjet that may be difficult to predict with models.

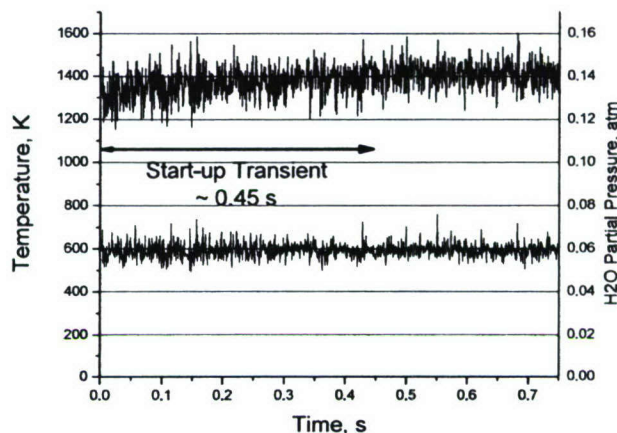


Figure 2.4.11. Temperature and water concentration data obtained with WMS-2*f* showing a portion of the start-up transient after combustor ignition. 1392/1469 nm line pair. $\phi = 1.20$.

Figure 2.4.12 shows measurements of mean temperature as a function of fuel/air equivalence ratio using the 1392/1469 nm line pair. The error bars represent a single standard deviation of the data at 2 kHz. Also shown is the temperature calculated by a 1-D model developed by the researchers at Wright-Patterson AFB. The model solves the 1-

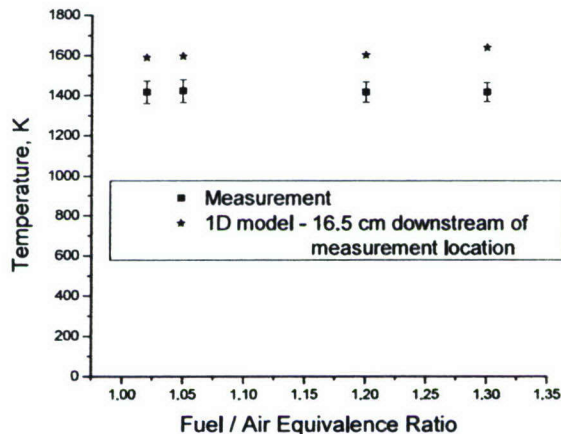


Figure 2.4.12. Average measured temperature and 1-D simulated temperature (6.5 inches downstream of measurement location) versus combustor fuel/air equivalence ratio. Error bars represent standard deviation at 2 kHz sample rate. 1392/1469 nm line pair.

D conservation equations incorporating reactant mass flow rate, load cell force, heat loss, and pressure data from each run. Some deviation between the simulated and measured temperatures is expected because the model predicts the temperature at the end of the combustor, which is 16.5 cm downstream from the measurement location. Two competing phenomena occur in the scramjet between the measurement location and the end of the combustor. The duct diverges, causing pressure drop and a corresponding

temperature drop, and heat release still may be occurring as the gases pass the measurement location, which will cause an increase in temperature. Another factor to consider is that the beam path for the laser measurements may be positioned at an elevation that is not representative of the 1-D temperature. The key aspect of Fig. 2.4.12 is that the trend of the measured temperature matches that of the simulated temperature. Measurements of this nature are helpful to determine optimal scramjet run parameters such as fuel/air ratio or to characterize the efficiency of various flame holder designs or engine components.

Current Status

A second-generation scanned WMS-2f diode laser absorption sensor has been designed, built, and tested in the laboratory for further measurement campaigns in Test Cell 22 at the AFRL Propulsion Directorate, Wright-Patterson, AFB, OH. This system, termed WMS-2f/1f, incorporates a new method of signal normalization that accounts for beam steering, window fouling, and other noise sources. In addition, this normalization enables quantitative measurements without *in situ* calibration. The first measurements using this new sensor system are planned for December 2006.

2.4.3. Mid-IR measurements of fuels using diode lasers

In our recent AFOSR-sponsored work we successfully demonstrated quantitative ethylene and propane sensing using commercially available near-infrared (NIR) tunable diode laser sources [2.4.6]. However, hydrocarbon absorption at these NIR wavelengths uses transitions in the vibrational overtone and combination bands where the absorption cross sections are relatively small and that become even smaller and more problematic for the larger and more complex hydrocarbon species found in jet fuels. The recent extension of solid-state tunable laser technology into the mid-infrared (MIR) now provides the opportunity for absorption measurements of hydrocarbons using transitions in the fundamental C-H stretching vibrational mode where the absorption cross section is much larger. Using this much stronger absorption strength, new and much more sensitive diagnostic techniques can be anticipated. However, these techniques will differ from those developed previously (in the NIR) for small hydrocarbons with discrete spectra owing to the broader spectral features of relevant large hydrocarbon molecules. Recently we have begun to investigate a novel dual-wavelength differential absorption (DWDA) fuel sensor that we believe holds high potential. Our first proof-of-concept experiments on n-dodecane are described below.

Background

The enabling technology for this new fuel sensing strategy is the recent commercial development of all-solid-state, wavelength-tunable mid-IR laser sources using difference-frequency-generation (DFG) and our acquisition of a prototype device using support from our AFOSR Defense University Instrumentation Program (DURIP) grant. The ability to tune or select the specific sensor wavelength is very important for mid-IR absorption sensing. Tunability allows selection of a wavelength that avoids potential interference from structured absorption of water vapor combustion products. Wavelength choice also allows the absorption strength to be selected from the broad unstructured hydrocarbon vibrational absorption features for maximum dynamic range of the absorption signal for the expected range of fuel concentration and path length.

The spectroscopy of complex hydrocarbon fuel species is significantly different than observed for small polyatomic compounds such as H_2O , CH_4 , C_2H_4 , or C_2H_2 , which all have well-resolved rotational-state-specific structure. The rotational structure in complex hydrocarbon fuel molecules is spaced very closely and blended by pressure and Doppler broadening into unresolved absorption features. The broad structure of the absorption spectrum motivates our work to develop a differential absorption strategy where measurements are made at two colors in one of these broad absorption features. Differential absorption measurements will allow quantitative measurement of the vapor concentration even with attenuation of the laser beam from window fouling, scattering losses, or beam steering.

Wavelength-tunable mid-IR laser source using DFG

The fiber optics and lasers developed for telecommunications in the NIR have the mechanical robustness needed for routine sensing in aeroengine research, and our current AFOSR-sponsored research has exploited these components for successful measurements of time-resolved gas temperature in scramjet and gas turbine combustors [2.4.1].

Recently non-linear conversion techniques have extended lasers based on these robust optical components into the mid-IR. Wavelength-tunable mid-IR lasers using difference-frequency-generation in periodically poled lithium niobate (PPLN) have been used for the past decade for sensitive detection of trace species in the atmosphere, but virtually all of this work has required use of large pulsed lasers. The availability of continuous (cw) sources has remained an elusive, unfulfilled development goal.

Recently, however, a cw source using tunable diode lasers and fiber amplifiers was demonstrated, allowing reduced power consumption for balloon-borne measurements. This laser design proved quite stable and robust, and a similar architecture now is being commercialized by a San Francisco start-up company (NovaWave). The laser design, illustrated in Fig. 2.4.13, fiber-amplifies a NIR wavelength-tunable diode laser (seed) and combines this light in a polarization-maintaining fiber with a powerful single-frequency diode laser. These two near-IR laser wavelengths are mixed in a periodically poled lithium niobate (PPLN) crystal to produce laser light at the difference frequency (here near 3.4 μm in the mid-IR). The mid-IR light can be tuned in wavelength by changing the wavelength of the near-IR seed laser, and when this change is done by rapidly (thus far we have demonstrated up to 100 kHz) alternating between two separate near-IR seed lasers, as illustrated in Fig. 2.4.13, the output consists of a beam that alternates between two-colors of mid-IR light along a single optical path. The current laser, recently procured on our AFOSR DURIP grant and based on a wavelength-dithering concept we suggested to the vendor, enables us to separate the two mid-IR colors by $\sim 10 \text{ cm}^{-1}$, which is well-suited for the initial feasibility measurements described below on evaporating n-dodecane vapor. Custom PPLN crystals would enable this color separation to be enhanced significantly, enabling further advances in sensor performance for cases where increased spectral separation would yield better vapor sensing capability in the presence of liquid fuel droplets.

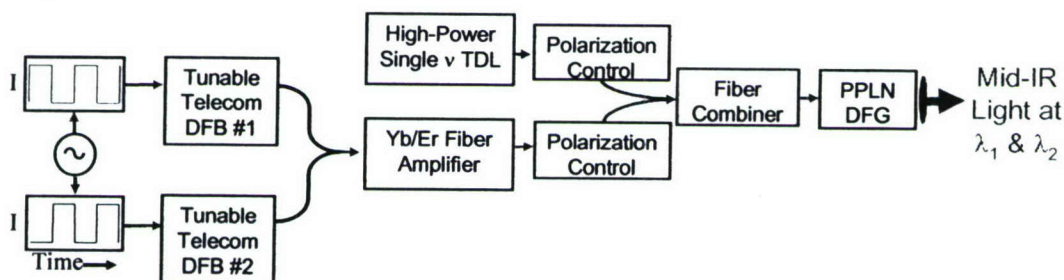


Figure 2.4.13. Architecture of all solid-state two-color DFG mid-IR light source.

Dual-wavelength differential absorption to suppress aerosol interference

We demonstrated the dual-wavelength differential-absorption (DWDA) sensor concept using this novel two-color mid-infrared (mid-IR) laser. The total Beer's law extinction at each frequency ν (color) is the sum of vapor absorption and droplet scattering:

$$\left(\frac{I}{I_0} \right)_{\nu} = \exp[-\alpha_{\text{vapor}}(\nu) - \tau_{\text{droplets}}(\nu)]$$

Thus if we measure the extinction at two laser frequencies, ν_1 and ν_2 , solving for the vapor absorption reduces to the solution of two equations with two unknowns. This DWDA sensing concept is able to extract the vapor absorption signal from strong interference attenuation due to scattering from the aerosol droplets during evaporation of shock-heated n-dodecane aerosol. First we examine the absorption spectrum to select the laser frequencies. The left panel of Fig. 2.4.14 shows the mid-IR absorption spectrum of n-dodecane in the region of the C-H stretching vibration. We select two laser frequencies, $\nu_1=2916\text{cm}^{-1}$ and $\nu_2=2926\text{cm}^{-1}$, to maximize the difference in the absorption coefficient between the two laser colors, as illustrated on the plot. Then we must understand the dependence of the absorption spectrum on temperature (and pressure). The measured pressure dependence is small and can be neglected for n-dodecane for $P<10\text{atm}$; however, there is a significant temperature dependence, as illustrated in the right panel of Fig. 2.4.14 where the differential absorption coefficient is shown versus T.

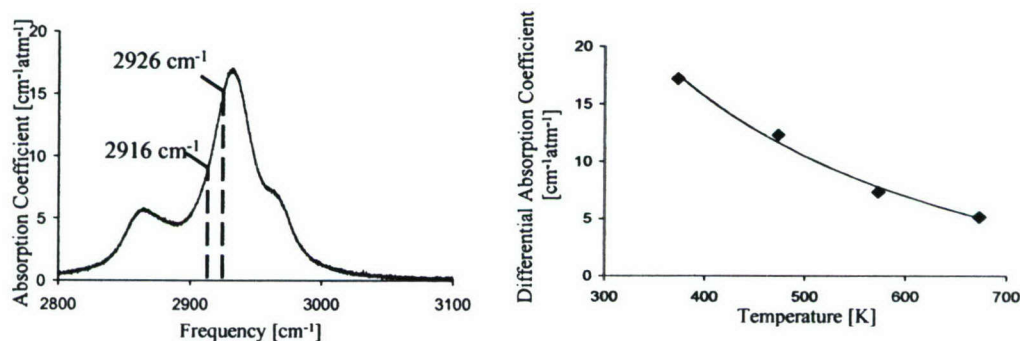


Figure 2.4.14. Left panel: absorption coefficient of n-dodecane vapor dilute in 1 atmosphere of nitrogen measured at 675K via FTIR; Right panel: differential absorption coefficient versus gas temperature for n-dodecane vapor at 2916 and 2926 cm^{-1} .

An aerosol of n-dodecane is prepared via an ultrasonic nebulizer and mixed with argon in Stanford University’s aerosol shock tube facility, as illustrated in Fig. 2.4.15. DWDA of the two-color mid-IR laser extinction is used to extract the vapor concentration of n-dodecane, and extinction of the NIR laser is used to monitor the vapor

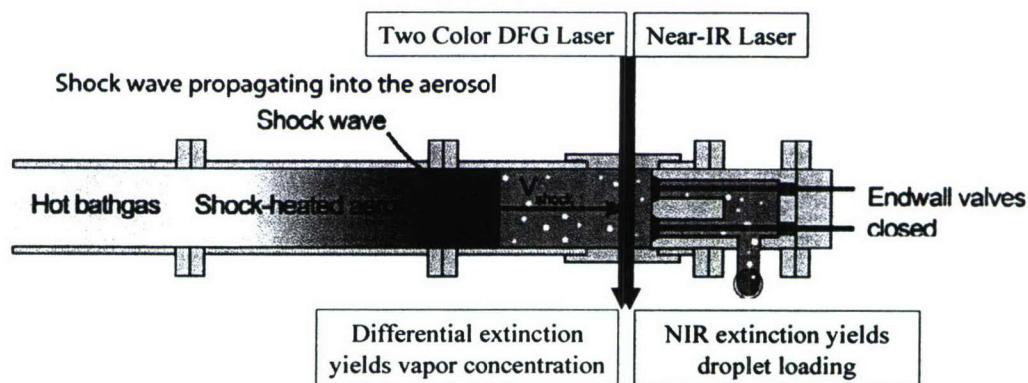


Figure 2.4.15. Stanford’s aerosol shock tube with the mid-IR DWDA diagnostic plus NIR extinction to monitor the droplet loading.

loading. The two-color mid-IR laser switches between $\nu_1=2916\text{cm}^{-1}$ and $\nu_2=2926\text{cm}^{-1}$ at 100 kHz, thus enabling differential absorption measurements with 10 μs time resolution. The measurement is shown in Fig. 2.4.16 for a pre-shock pressure of 0.22 atm and pre-shock temperature of 300K. Before the shock-heating, the aerosol scattering reduces the laser transmission by 48%, as seen by the NIR transmission. Even with this significant aerosol scattering interference, the DWDA measurement recovers the small 300K vapor pressure ($P_{\text{vapor}}=0.16$ Torr) of n-dodecane. When the incident shock arrives, the aerosol-laden gas is compressed to a post-shock pressure of 0.78 atm and post-shock temperature of 436K. The aerosol loading increases because of shock compression, and the transmission of the NIR laser light drops below 20% (i.e., the interference extinction is greater than 80%), as seen in Fig. 2.4.16. However, at the post-shock temperature of 436K, the aerosol rapidly evaporates, and the time-resolved increase in the n-dodecane vapor is monitored successfully by DWDA, as shown in the figure. When the droplets are evaporated completely the NIR transmission recovers to 100%, and the DWDA measures the vapor initially contained in the droplets plus the initial 300K vapor pressure.

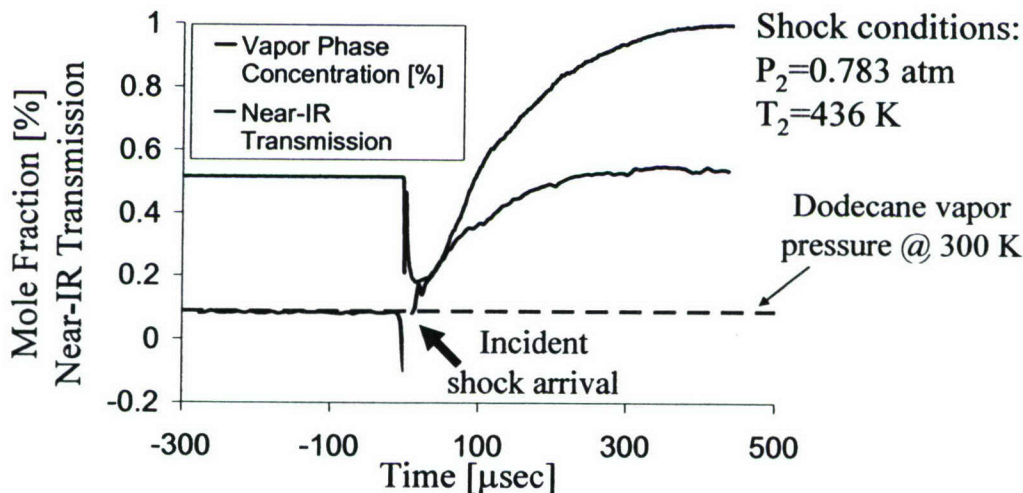


Figure 2.4.16. Shock-heated n-dodecane aerosol monitored via mid-IR DWDA for vapor mole fraction of do-decane and NIR transmission to monitor aerosol loading: Test gas at 300K, $P=0.22$ atm, $\chi_{\text{vapor}}=0.09\%$ with post-shock $T=436\text{K}$, $P=0.78\text{atm}$ and final $\chi_{\text{vapor}}=0.54\%$.

Current Status

The measurements shown in Fig. 2.4.16 formed the cornerstone of a presentation at the 31st International Combustion Symposium last summer [2.4.7]. We believe this new concept for diode laser-based mid-infrared sensing offers significant potential for sensing hydrocarbon fuels for fundamental chemistry experiments, laboratory combustion experiments, and practical aeroengine ground test.

References for Advanced Wavelength-Multiplexed Absorption Sensors

- [2.4.1] Ronald K. Hanson (Invited) and J.B. Jeffries, "Diode laser sensors for ground testing," *25th Aerodynamic Measurement Technology and Ground Testing Conference*, American Institute of Aeronautics and Astronautics, AIAA 2006-3441.
- [2.4.2] S.T. Sanders, J. Wang, J.B. Jeffries, R.K. Hanson, "Diode-laser absorption sensor for line-of-sight gas temperature distributions," *Applied Optics* **40** (2001) 4404-4415.
- [2.4.3] M. Gruber, J. Donbar, K. Jackson, T. Marthur, R. Baurle, D. Eklund, and C. Smith, "Newly developed direct-connect high-enthalpy supersonic combustion research facility," *Journal of Propulsion and Power* **17**, 2001, pp. 1296-1304.
- [2.4.4] L.C. Philippe and R.K. Hanson, "Laser diode wavelength-modulation spectroscopy for simultaneous measurement of temperature, pressure, and velocity in shock-heated oxygen flows," *Applied Optics* **32**, 1993, pp. 6090-6103.
- [2.4.5] J.T.C. Liu, J.B. Jeffries, and R.K. Hanson, "Wavelength modulation absorption spectroscopy with $2f$ detection using multiplexed diode lasers for rapid temperature measurements in gaseous flows," *Applied Physics B* **78**, 2004, pp. 503-511.
- [2.4.6] L. Ma, S.T. Sanders, J.B. Jeffries, and R.K. Hanson, "Monitoring and control of a pulse detonation engine using a diode-laser fuel concentration and temperature sensor," *Proceedings of the Combustion Institute* **29** (2002) 161-166.
- [2.4.7] A.E. Klingbeil, J.B. Jeffries, and R.K. Hanson, "Tunable mid-IR laser absorption for time-resolved hydrocarbon fuel measurements," *Proc. Combustion Institute* **31** (2007) 807-815.

2.5 Photophysics studies in support of tracers for fuel imaging

Background

PLIF imaging of tracer molecules has proven to be a powerful diagnostic for investigating the behavior of fuels, for example in mixing and combustion. PLIF imaging of acetone, pioneered at Stanford with AFOSR support, is widespread owing to its ease of use and, importantly, to its simple interpretation for isobaric and isothermal flows. Similarly, 3-pentanone, a slightly larger member of the ketone family, has seen growing use, particularly in internal combustion engines. Past work at Stanford has sought build a fundamental understanding of the photophysics of these tracers to enable their quantitative use in flows with varying pressure, temperature, and composition. Accurate databases for the absorption and fluorescence behavior of these two ketones have thus been acquired and physically realistic photophysical models assembled and fit to the available experimental data. These models, in turn, have been used to identify new diagnostic strategies for simultaneously measuring the tracer concentration and temperature, as well as to enable quantitative application of PLIF imaging over a range of pressures and temperatures. This body of work on tracer photophysics and modeling has had considerable impact internationally on combustion diagnostics.

Current Status of Toluene Photophysics

During the past AFOSR-grant period, we have begun to extend this work on the photophysics of fuel tracers to include toluene, an aromatic compound that is present in jet fuel and is commonly selected as the aromatic component in surrogate mixtures of hydrocarbons used to simulate behavior of jet fuels. While we are still in a relatively early phase of these studies with toluene, we already have acquired a database for the absorption spectrum as a function of temperature and for the fluorescence yield at two selected excitation wavelengths (248 nm and 266 nm) but essentially limited to nitrogen as a bath gas. This work has documented a very strong temperature dependence of the toluene LIF signal, shown in Fig. 2.5.1, which suggests exciting potential for a new, highly sensitive PLIF temperature diagnostic [2.5.1]. There is also a very strong dependence of the toluene fluorescence on oxygen concentration, which leaves open the

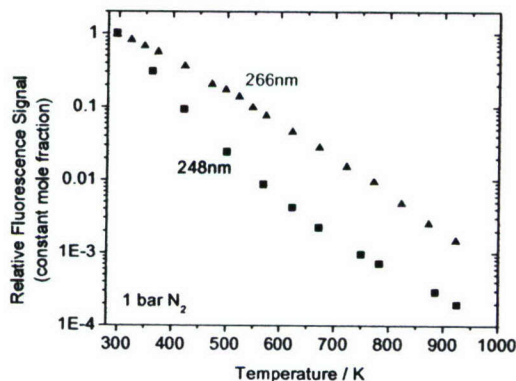


Figure 2.5.1. Relative toluene LIF signal from 248-nm and 266-nm excitation as a function of temperature at 1 bar total pressure (diluted with nitrogen). [2.5.1]

hope of simultaneously imaging temperature and fuel-air ratio [2.5.2]. As an illustrative example of the promise of a toluene PLIF diagnostic, Fig. 2.5.2 provides a single-shot, 2-D temperature measurement image acquired for a heated cylinder in a uniform nitrogen flow seeded with toluene. The high precision of the measurement enables a resolution of temperature differences of about 5 K.

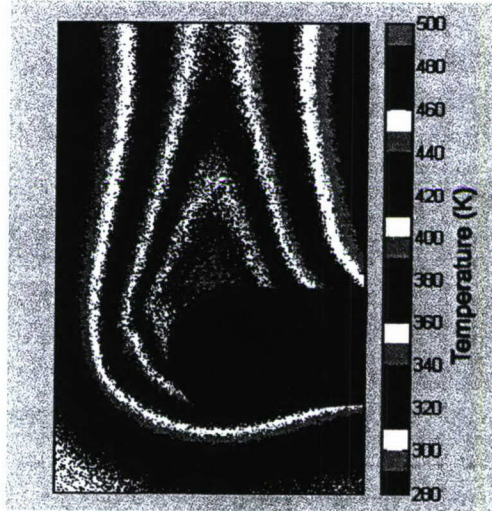


Figure 2.5.2. Single-shot PLIF temperature image of uniform nitrogen flow around a heated cylinder using a toluene tracer. The laser sheet is incident from the left side of the image.

Research into High-Temperature and -Pressure Toluene Photophysics

To characterize the PLIF signal, we utilize the fluorescence equation:

$$S_f \propto E \cdot n \cdot \sigma(\lambda, T) \cdot \phi(\lambda, T, p)$$

where E is laser energy, n is the tracer number density, σ is the absorption cross section, and ϕ is the fluorescence quantum yield. Any quantitative PLIF diagnostic clearly depends on knowledge of the absorption cross section and the fluorescence quantum yield. Measurements of the variations in the absorption cross section and the fluorescence quantum yield with respect to pressure, temperature, and composition are thus of special importance to the development of a quantitative and optimized toluene PLIF diagnostic, and very little data of this type currently exist for toluene.

As stated previously, our preliminary measurements of the fluorescence quantum yield in toluene and its variation with temperature are conducted in nitrogen bath gas at a pressure of 1 atm. The experimental setup used to make these measurements is shown in Fig. 2.5.3, and recently we have designed modifications to this test cell to accommodate a much wider range of pressures and temperatures.

The tracer (e.g. toluene) is introduced into the carrier gas using a saturating percolator. The seeded gas subsequently flows into an optically accessible cell, where it is excited by the appropriate laser. The fluorescence signal is measured via either a PMT or a CCD camera mounted on a spectrograph. By using a furnace with the cell, the effect

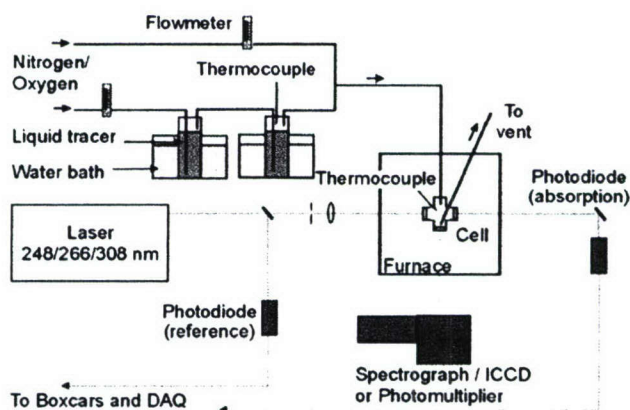


Figure 2.5.3. Experimental setup for measuring absorption cross section and fluorescence quantum yield of tracers as a function of temperature.

of increasing temperature on the fluorescence signal can be measured. By increasing the internal pressure of the cell, the effect of pressure of fluorescence signal can be measured. This measurement technique, including a novel Rayleigh scattering approach for absolute calibration of fluorescence yield, is developed in work on ketone fluorescence [2.5.3] and has worked well in our initial work with toluene.

Semi-Empirical Fluorescence Model for Ketone and Aromatic Tracers

A validated, physics-based model for the fluorescence quantum yield is critical for the development of successful diagnostic strategies. The fluorescence signal can be characterized using the fluorescence equation:

$$S_f \propto E \cdot n \cdot \sigma(\lambda, T) \cdot \phi(\lambda, T, p)$$

The critical information needed is embodied in the absorption cross section and the fluorescence quantum yield. A model of fluorescence quantum yield not only will contribute to the understanding of the processes underlying PLIF, but also will allow for the prediction of fluorescence behavior and optimization of diagnostic strategies for various conditions. Our past work to model the fluorescence quantum yield for acetone and 3-pentanone has contributed to the expanding use of ketone fluorescence in the PLIF diagnostic arena [2.5.4].

Fig. 2.5.4 diagrams our current conceptualization of the fluorescence process developed for ketones and extended for toluene. The laser photon excites the molecule from the S_0 state to the S_1 state. In the S_1 state, in addition to fluorescence, the molecule could undergo several processes. Intramolecular vibrational redistribution (IVR) redistributes the vibrational energy among all the levels of S_1 without changing total vibrational energy. IVR also affects intersystem crossing (ISC) and internal conversion (IC) rates, as these rates depend on the vibrational energy in the S_1 state. In ISC, the molecule goes from the excited state S_1 to the triplet state T_1 . In IC, the molecule goes from the S_1 state back to the S_0 state via the upper vibrational levels of the S_0 state. In addition, there is potential for collisions with oxygen molecules to promote further transfer of the toluene molecule to the S_0 and T_1 states through formation of short-lived molecular complexes. Besides fluorescence, none of these processes emit photons, so the

sole source of signal is fluorescence. The variation of these competing processes with pressure, temperature, and bath gas composition holds the key to allowing use of the fluorescence signal as a quantitative gasdynamic diagnostic.

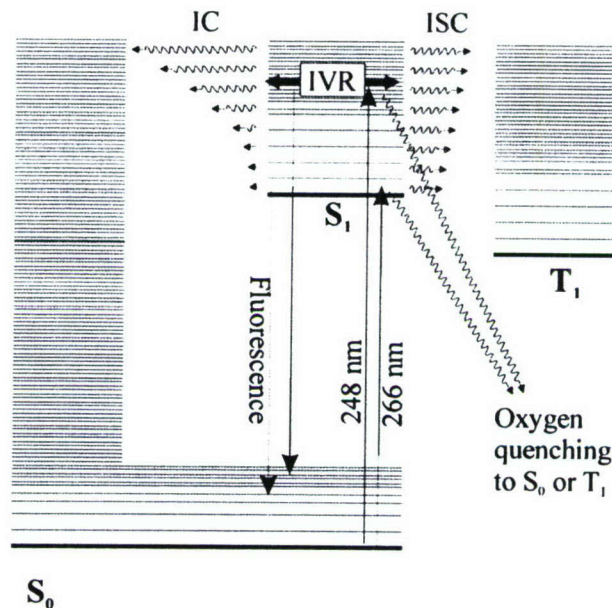


Figure 2..5.4. Fluorescence energy diagram for toluene.

Tracer Photophysics References

- [2.5.1] W. Koban, J.D. Koch, R.K. Hanson, C. Schulz, "Absorption and fluorescence of toluene at elevated temperatures," *Physical Chemistry Chemical Physics* **6** (2004) 2940-2945.
- [2.5.2] W. Koban, J.D. Koch, R. K. Hanson, C. Schulz, "Oxygen quenching of toluene fluorescence at elevated temperatures," *Applied Physics B* **80** (2005) 777-784.
- [2.5.3] J.D. Koch, W. Koban, C. Schulz, R.K. Hanson, "Rayleigh-calibrated fluorescence quantum yield measurements of acetone and 3-pentanone," *Applied Optics* **43** (2004) 5901-5910.
- [2.5.4] M.C. Thurber, F. Grisch, B.J. Kirby, M. Votsmeier, R.K. Hanson, "Measurements and modeling of acetone laser-induced fluorescence with implications for temperature-imaging diagnostics," *Applied Optics* **37** (1998) 4963-4978.

3.0 Publications and Presentations

The results of the AFOSR-sponsored research were published in thirty-eight archival and AIAA papers, seven PhD theses, and forty-three presentations and invited lectures.

3.1 AFOSR SPONSORED PUBLICATIONS 2004-2006

REVIEWED AND AIAA PUBLICATIONS 2004

1. J.T.C. Liu, J.B. Jeffries, and R.K. Hanson, "Wavelength modulation absorption spectroscopy for combustion temperature measurements using multiplexed near-infrared diode lasers," paper presented at *42nd Aerospace Sciences Meeting* (2004) American Institute of Aeronautics and Astronautics, AIAA-2004-0647.
2. T. Lee, J.B. Jeffries, R.K. Hanson, W.G. Bessler, and C. Schulz, "Carbon Dioxide UV Laser-Induced Fluorescence Imaging in High-Pressure Flames," *42nd Aerospace Sciences Meeting* (2004) American Institute of Aeronautics and Astronautics, AIAA-2004-0386.
3. R.K. Hanson and J.B. Jeffries, "Advances in laser-based sensors for propulsion systems," *24th AIAA Aerodynamic Measurement Technology and Ground Testing Conference* (2004), American Institute of Aeronautics and Astronautics, AIAA-2004-2476.
4. J.D. Koch, W. Koban, C. Schulz, R.K. Hanson, "Rayleigh-calibrated fluorescence quantum yield measurements of acetone and 3-pentanone," *Applied Optics* **43** (2004) 5901-5910.
5. W. Koban, J.D. Koch, R.K. Hanson, C. Schulz, "Absorption and fluorescence of toluene vapor at elevated temperatures," *Physical Chemistry Chemical Physics* **6** (2004) 2940-2945.
6. M.A. Oehlschlaeger, D.F. Davidson, J.B. Jeffries, and R.K. Hanson, "Ultraviolet absorption cross sections of hot carbon dioxide," *Chemical Physics Letters* **399** (2004) 490-495.
7. T. Lee, W. G. Bessler, C. Schulz, M. Patel, J.B. Jeffries, and R.K. Hanson, "UV planar laser induced fluorescence imaging of hot carbon dioxide in a high-pressure flame," *Applied Physics B* **79** (2004) 427-430.
8. J.T.C. Liu, J.B. Jeffries, and R.K. Hanson, "Wavelength modulation absorption spectroscopy with 2f detection using multiplexed diode lasers for rapid temperature measurements in gaseous flows," *Applied Physics B* **78** (2004) 503-511.
9. H. Li, R.K. Hanson, and J.B. Jeffries, "Diode laser induced infrared fluorescence of water vapor," *Journal Measurement Science and Technology* **15** (2004) 1285-1290.
10. T. Rossmann, M.G. Mungal, and R.K. Hanson, "Mixing efficiency measurements using a modified cold-chemistry technique," *Experiments in Fluids* **37** (2004) 566-576.

11. J.T.C. Liu, J.B. Jeffries and R.K. Hanson, "Large-modulation-depth 2f spectroscopy with diode lasers for rapid temperature and species measurements in gases with blended and broadened spectra," *Applied Optics* **43** (2004) 6500-6509.

REVIEWED AND AIAA PUBLICATIONS 2005

12. Xiang Liu, Xin Zhou, Jay B. Jeffries and Ronald K. Hanson, "Experimental study of H₂O spectroscopic parameters in the near-IR, " *43rd AIAA Aerospace Sciences Meeting* (2005), American Institute of Aeronautics and Astronautics, AIAA-2005-0829.
13. J.B. Jeffries, C. Schulz, D.W. Mattison, M.A. Oelschlaeger, W.G. Bessler, T. Lee, D.F. Davidson, and R.K. Hanson, "UV absorption of CO₂ for temperature diagnostics of hydrocarbon combustion applications," *Proceedings of the Combustion Institute* **30** (2005) 1591-1599.
14. W. Koban, J. Koch, V. Sick, N. Wermuth, R.K. Hanson, and C. Schulz, "Predicting LIF signal strength for toluene and 3-pentanone under transient temperature and pressure conditions," *Proceedings of the Combustion Institute* **30** (2005) 1545-1553.
15. L. Ma, R.K. Hanson, "Measurement of aerosol size distribution functions by wavelength-multiplexed laser extinction," *Applied Physics B* **81** (2005) 567-576.
16. W. Koban, J.D. Koch, R.K. Hanson, C. Schulz, "Toluene LIF at elevated temperatures: implications for fuel-air ratio measurements," *Applied Physics B*. **80** (2005) 147-150.
17. W. Koban, J.D. Koch, R.K. Hanson, C. Schulz, "Oxygen quenching of toluene fluorescence at elevated temperatures," *Applied Physics B* **80** (2005) 777-784.
18. A.E. Klingbeil, J.B. Jeffries, R.K. Hanson, C. Brophy, and J. Sinibaldi, "Mid-IR laser absorption measurements of ethylene in a pulsed detonation engine," *41st Joint Propulsion Conference*, AIAA 2005-4375.
19. G.B. Rieker, J.T.C. Liu, J.B. Jeffries, R.K. Hanson, T. Mathur, M.R. Gruber, and C. Carter, "Wavelength-multiplexed tunable diode laser sensor for temperature and water concentration in a scramjet combustor," *41st Joint Propulsion Conference*, AIAA 2005-3710.
20. M.A. Oehlschlaeger, D.F. Davidson, J.B. Jeffries, and R.K. Hanson, "Carbon dioxide thermal decomposition: observation of incubation," *Zeitschrift für Physikalische Chemie* **219** (2005) 555-567.
21. W. Juchmann, J. Luque, and J.B. Jeffries, "Two-photon laser-induced fluorescence of atomic hydrogen in a diamond depositing dc-arcjet," *Applied Optics* **44** (2005) 6644-6652.
22. M.A. Oehlschlaeger, D.F. Davidson, J.B. Jeffries, "Temperature measurements behind shock waves using ultraviolet laser absorption of carbon dioxide," *Applied Optics* **44** (2005) 6599-6605.

23. J.T.C. Liu, G.B. Rieker, J.B. Jeffries, R.K. Hanson, M.R. Gruber, C.D. Carter, and T. Mathur, "Near-infrared diode laser absorption diagnostics for temperature and water vapor in a scramjet combustor, *Applied Optics* **44** (2005) 6701-6711.
24. T. Lee, W.G. Bessler, H. Kronemayer, C. Schulz, J.B. Jeffries, "Quantitative temperature measurements in high-pressure flames with multi-line NO-LIF thermometry," *Applied Optics* **44** (2005) 6718-6728.

REVIEWED AND AIAA PUBLICATIONS 2006

25. A. Ben-Yakar, M.G. Mungal, and R.K. Hanson, "Time evolution and mixing characteristics of hydrogen and ethylene transverse jets in supersonic crossflows," *Physics of Fluids* **16** (2006) 026101, 16 pages.
26. Xiang Liu, Jay B. Jeffries, Ronald K. Hanson, "Measurement of non-uniform temperature distribution measurement using line-of-sight absorption spectroscopy," *44th Aerospace Sciences Meeting*, (2006) American Institute of Aeronautics and Astronautics, AIAA 2006-834.
27. Ronald K. Hanson (Invited) and J.B. Jeffries, "Diode laser sensors for ground testing," *25th Aerodynamic Measurement Technology and Ground Testing Conference*, American Institute of Aeronautics and Astronautics, AIAA 2006-3441.
28. D.A. Rothamer and R.K. Hanson, "Visualization of high-speed flows using infrared planar laser induced fluorescence of CO and CO₂," *42nd Joint Propulsion Conference*, American Institute of Aeronautics and Astronautics, AIAA 2006-4300.
29. H. Li, X. Zhou, J.B. Jeffries, R.K. Hanson, "Sensing and control of combustion instabilities in swirl-stabilized combustors using a diode laser," *42nd Joint Propulsion Conference*, American Institute of Aeronautics and Astronautics, AIAA 2006-4395.
30. A.E. Klingbeil, J.B. Jeffries, and R.K. Hanson, "Temperature- and pressure-dependent absorption cross-sections of gaseous hydrocarbons at 3.39 μ m," *Measurement Science and Technology* **17** (2006) 1950-1957.

REVIEWED PUBLICATIONS TO APPEAR IN 2007

31. T. Lee, J.B. Jeffries, and R.K. Hanson, "Experimental evaluation of strategies for quantitative laser-induced-fluorescence imaging of nitric oxide in high-pressure flames (1–60bar)," *Proceedings of the Combustion Institute* **31** (2007) 757-764.
32. A.E. Klingbeil, J.B. Jeffries, and R.K. Hanson, "Tunable mid-IR laser absorption for time-resolved hydrocarbon fuel measurements," *Proceedings of the Combustion Institute* **31** (2007) 807-815.
33. H. Li, X. Zhou, J.B. Jeffries, and R.K. Hanson, "Active control of lean blowout in a swirl-stabilized combustor using a tunable diode laser," *Proceedings of the Combustion Institute* **31** (2007) 3215-3223.
34. X. Liu, X. Zhou, J. B. Jeffries and R. K. Hanson, "Experimental study of H₂O spectroscopic parameters in the near-IR (6940-7440 cm⁻¹) for Gas Sensing applications at elevated temperature," *Journal of Quantitative Spectroscopy and Radiative Transfer* **103**(2007) 565-577.

35. G.B. Rieker, X. Liu, H. Li, J.B. Jeffries, R.K. Hanson, "Measurements of near-IR water vapor absorption at high pressure and temperature," *Applied Physics B* (2007) in press; on-line DOI 10.1007/s00340-006-2523-4.
36. H. Li, X. Zhou, J.B. Jeffries, R.K. Hanson, "Sensing and control of combustion instabilities in swirl-stabilized combustors using a diode laser," *AIAA Journal*, (2007) in press.
37. X. Liu, J.B. Jeffries, R.K. Hanson, "Measurement of non-uniform temperature distributions using line-of-sight absorption spectroscopy," *AIAA Journal* (2007) in press.
38. A.E Klingbeil, J. B. Jeffries, R.K. Hanson, "Design of a fiber-coupled mid-IR fuel sensor for pulse detonation engines," *AIAA Journal* (2007) in press.

3.2 PhD THESIS WITH AFOSR SUPPORT

1. J.T.C. Liu, "Near-Infrared Diode Laser Absorption Diagnostics for Temperature and Species in Engines," Ph.D. Thesis, Department of Mechanical Engineering, Stanford, CA, October, 2004; Thermosciences Division Report 154, <http://navier.stanford.edu/tsd/TSD-154.pdf>.
2. Jon Koch, "Fuel Tracer Photophysics for Quantitative Planar Laser-Induced Fluorescence," Ph.D. Thesis, Department of Mechanical Engineering, Stanford, CA, May, 2005; Thermosciences Division Report 159, <http://navier.stanford.edu/tsd/TSD-159.pdf>.
3. M. A. Oehlschlaeger, "Shock Tube Studies of Thermal Decomposition Reactions using Ultraviolet Laser Absorption Spectroscopy," Ph.D. Thesis, Department of Mechanical Engineering, Stanford, CA, June, 2005; Thermosciences Division Report 160, <http://navier.stanford.edu/tsd/TSD-160.pdf>.
4. Ma Lin, "Laser Diagnostics for Simultaneous Vapor and Droplet Measurement in Sprays," Ph.D. Thesis, Department of Mechanical Engineering, Stanford, CA, December, 2005; Thermosciences Division Report 162, <http://navier.stanford.edu/thermosciences/TSD-162.pdf>.
5. Dan Mattison, "Development and Application of Laser-Based Sensors for Harsh Combustion Environments," Ph.D. Thesis, Department of Mechanical Engineering, Stanford, CA, March, 2006; Thermosciences Division Report 164, <http://navier.stanford.edu/thermosciences/TSD-164.pdf>.
6. Tonghun Lee, "Strategies For Nitric Oxide Laser-Induced-Fluorescence In High-Pressure Combustion Systems," Ph.D. Thesis, Department of Mechanical Engineering, Stanford, CA, March, 2006; Thermosciences Division Report 165, <http://navier.stanford.edu/thermosciences/TSD-165.pdf>.
7. Xiang Liu, "Line-of-Sight Absorption of H₂O Vapor: Gas Temperature Sensing in Uniform and Nonuniform Flows," Ph.D. Thesis, Department of Mechanical Engineering, Stanford, CA, June, 2006; Thermosciences Division Report 168, <http://navier.stanford.edu/thermosciences/TSD-168.pdf>.

3.3 AFOSR SPONSORED PRESENTATIONS 2004-2006

MEETING PRESENTATIONS 2004

1. Two presentations at the AIAA Aerospace Science Meeting (papers listed above)
3. One presentation at the AIAA AMT and Ground Test Meeting (paper listed above)
4. Three oral presentations at the 30th International Symposium on Combustion in Chicago (reviewed papers listed as published in 2005)
7. W. Koban, J.D. Koch, R. K. Hanson, and C. Schulz, "FARLIF: Myths and Reality," poster at the 30th *International Symposium on Combustion in Chicago*, July 2004.
8. W.G. Bessler, H. Kronemayer, C. Schulz, T. Lee, J.B. Jeffries, R.K. Hanson, "Quantitative multi-line NO-LIF temperature imaging in flames over a wide pressure range," *Laser Applications to Chemical, Environmental, and Atmospheric Analysis*, Optical Society of America, Annapolis, Feb. 2004.
9. E. Barbour, M.A. Oelschlaeger, D.W. Mattison, D.F. Davidson, C. Schulz, J.B. Jeffries, R.K. Hanson, "UV absorption of CO₂ for temperature diagnostics," *Laser Applications to Chemical, Environmental, and Atmospheric Analysis*, Optical Society of America, Annapolis, Feb. 2004.
10. J.B. Jeffries (invited), "Tunable diode laser sensors for practical combustion applications," *Conference on Lasers and Electro-Optics*, Optical Society of America, San Francisco, CA, May, 2004.

MEETING PRESENTATIONS 2005

11. One presentation at the AIAA Aerospace Sciences Meeting (paper listed above)
12. Two presentations at the AIAA JPC Conference (papers listed above)
13. D.W. Mattison, J.T.C. Liu, G.B. Rieker, J.B. Jeffries, R.K. Hanson, "Diode laser sensors for internal combustion and aeropropulsion engine applications," *Thermosciences Division Industrial Affiliates*, Stanford University, February, 2005.
14. T. Lee, W.G. Bessler, H. Kronemayer, C.Schulz, J.B. Jeffries, R.K. Hanson, "Quantitative temperature measurements in high-pressure flames with multi-line nitric oxide (NO)-LIF thermometry," *Joint Meeting of the US Sections of the Combustion Institute*, Philadelphia, PA, March, 2005.
15. R.K. Hanson, J.B. Jeffries, M.G. Allen, "Tunable diode laser absorption sensor applications to aeropropulsion testing," *NATO RSM-017 Applied Vehicle Technology Panel Specialists' Meeting on Recent Developments in Non-Intrusive Measurement Technology*, Budapest, Hungary, April, 2005; invited plenary lecture.
16. M. Gruber, D. Eklund, T. Mathur, J. Jeffries, "In-stream measurements at the exit of dual-mode hydrocarbon-fueled scramjet combustors," *40th Combustion Subcommittee, 28th Airbreathing Propulsion Subcommittee, 22nd Propulsion Systems Hazards Subcommittee, and 4th Modeling and Simulation Subcommittee Joint Meeting*, JANNAF, June 2005.

17. R.K. Hanson (invited) and J.B. Jeffries, "Advances in diode laser sensors for combustion and propulsion," *Western States Section Meeting of the Combustion Institute*, paper 05-01F Stanford, CA, October, 2005.

MEETING PRESENTATIONS 2006

18. One presentation at the AIAA Aerospace Sciences Meeting (paper listed above)
19. One presentation at the AIAA AMT and Ground Test Meeting (paper listed above)
20. Two presentations at the AIAA JPC Conference (papers listed above)
22. Three presentations at the 31st International Symposium on Combustion in Heidelberg Germany (reviewed papers listed as published in 2007)
26. Ronald K. Hanson (invited) and Jay B. Jeffries, "Advances in diode laser absorption sensors for combustion and propulsion," *Laser Applications to Chemical, Environmental, and Atmospheric Analysis*, Optical Society of America, Incline Village, CA, February, 2006.
27. R.K. Hanson and J.B. Jeffries, "Diode sensors for combustion and propulsion," 41st *Combustion Subcommittee*, 29th *Airbreathing Propulsion Subcommittee*, 23rd *Propulsion Systems Hazards Subcommittee*, JANNAF, San Diego, CA, December, 2006.

INVITED LECTURES 2004-2006

28. R.K. Hanson, "Advances in planar laser-induced fluorescence imaging and applications to combustion and propulsion," *JAXA*, Japan Space Agency, March, 2004.
29. R. K. Hanson, "Tunable diode lasers for sensing and control with applications in combustion and propulsion," *Tokyo Institute of Technology*, March 2004.
30. J.B. Jeffries, "Laser diagnostics for combustion and propulsion," *University of Duisburg-Essen*, Duisburg, Germany, April 2004
31. R.K.Hanson and J.B.Jeffries, "Advances in laser-based sensors for combustion research," *Sixth Symposium on Smart Control of Turbulence*, Tokyo, Japan, March, 2005; invited plenary lecture.
32. R.K. Hanson, "Diode laser sensors for combustion and propulsion applications," *Tokyo Institute of Technology*, March, 2005.
33. M. A. Oehlschlaeger, "Shock tube studies of thermal decomposition reactions using ultraviolet laser absorption spectroscopy," *Combustion Research Facility, Sandia National Laboratory*, Livermore, CA, May, 2005.
34. J. Koch, "Fuel tracer photophysics for quantitative planar laser-induced fluorescence," *Marquette University*, April, 2005.
35. J.B. Jeffries, "UV absorption of CO₂: opportunities for new combustion diagnostics," *Gordon Research Conference on Laser Diagnostics for Combustion*, August, 2005.

36. R.K. Hanson, "Optical Diagnostics for Hypersonic Flows," *University of Minnesota/AFOSR Workshop on Hypersonics*, September, 2005.
37. R.K. Hanson, "TDL Sensing for Augmentor Applications," Briefing at *WPAFB* November, 2005.
38. Ronald K. Hanson, "Laser-based Sensing and Control of Combustion Applications," *Workshop on Control and Enhancement of Combustion of High Velocity Vitiated Flows by Pulsed Discharges*, WPAFB, November, 2005.
39. Jay B. Jeffries and Ronald K. Hanson, "Advances in Diode Laser Sensors for Propulsion and Combustion," *AFRL*, WPAFB, March 2006.
40. Ronald K. Hanson, "Advances in Tunable Diode Laser (TDL) Sensing for Combustion and Propulsion," Keynote Address, *Georgia Tech Symposium in Honor of Professor Ben Zinn*, May, 2006.
41. Jay B. Jeffries and Ronald K. Hanson, "Optical Diagnostics for Practical Applications," *Instrumentation Roundtable on Ballistic Fire Initiation*, Joint Aircraft Survivability Program Review, Nellis AFB, September, 2006.
42. Ronald K. Hanson, "Applications of Laser Diagnostics to Combustion and Propulsion," *Lund University Laser Center*, Lund, University, September, 2006.
43. Ronald K. Hanson, "Advances in Diode Laser Sensors for Combustion and Propulsion," *Mechanical Engineering Seminar*, Purdue University, September, 2006.

4.0 Personnel

Individual researchers partially or fully supported by the program during the reporting period are listed below. All the work has been carried out in the High Temperature Gasdynamics Laboratory, in the Department of Mechanical Engineering, under the supervision of Professor R. K. Hanson.

Research Staff

Dr. Jay B. Jeffries, Senior Research Associate

Current Graduate Research Assistants

Brian Chung
Andrew Fahrland
Hejie Li
Gregory Rieker
David Rothamer
John Yoo

Ph.D Degrees Awarded 2004-2006 with Partial AFOSR Support

Jonathan Liu, 2004, currently NIH fellow, Stanford University
Jon Koch, 2005, currently Assistant Professor, Marquette University
M. A. Oehlschlaeger, currently Assistant Professor, Rensselaer Polytechnic Inst.
Lin Ma, 2005, currently Assistant Professor, Clemson University
Dan Mattison, 2006, currently with Exponent, Inc.
Tonghun Lee, 2006, currently Assistant Professor, Michigan State University
Xiang Liu, 2006, currently with Spectral Sensors, Inc.

Visitors Supporting the AFOSR Effort

Dr. Christof Schulz, 2004, Visiting Professor from the University of Heidelberg
Wieland Koban, 2004, Visiting Scientist from the University of Heidelberg
Wolfgang Bessler, 2004, Visiting Scientist from the University of Heidelberg

5.0 Significant Interactions

In addition to the interactions associated with the presentations and publications listed in Section 3 we have had numerous visitors to our laboratory during the contract period. Foreign visitors have come from the United Kingdom, Germany and Japan; industrial and national laboratory visitors have included representatives from:

Industry:

- Aerometrics
- Boeing
- Exxon
- NEL and NTT
- GE Research Laboratories
- Metrolaser
- Physical Sciences, Inc.
- Pratt and Whitney
- Rolls Royce
- TRW
- United Technologies
- Zolo Technologies

Government

- Air Force Research Laboratory (WPAFB)
- Army Research Laboratories (ARL)
- NASA Ames
- NASA Glen
- Sandia Livermore National Laboratory.

5.1 Interactions and Collaboration with AFRL

Stanford University hosted a workshop “Understanding Plasma Ignition” on January 9, 2004. Attendees included AFRL and AFOSR personnel; Skip Williams, AFRL/Geophysics; Campbell Carter, AFRL/Propulsion; Julian Tiskoff, AFOSR; and Michael Berman, AFOSR. AFOSR contractors were also participants including: Svetlana Starikovskaia, MIPT; Andrei Starikovskii, MIPT; Vincent McCoy, Cal Tech, Mark Kushner, U. Illinois; Robert Continetti, UCSD; Martin Gundersen, USC; Jay Jeffries and Ronald Hanson, Stanford University. In addition, one participant, Jose Sinibaldi, came from the Naval Postgraduate School in Monterey.

We collaborated with Dale Shouse of AFRL at WPAFB during 2003 on the writing of a paper describing the diode laser sensor measurements performed in the gas turbine sector test rig at AFRL in November of 2002. Jonathan Liu of Stanford University presented this paper at the AIAA Joint Propulsion Conference in Huntsville Alabama in July of 2003 and won AIAA’s Ground Test best paper award in June of 2004

A measurement campaign was conducted in September 2004 to perform diode laser sensing measurements in the scramjet combustor test facility at AFRL at Wright Patterson AFB, OH. This was the second set of measurements conducted in collaboration with Dr. Mark Gruber and Dr. Campbell Carter of AFRL. The improved

optical engineering used to match this sensor with the optical access in the test facility enabled major improvement in signal to noise. The results have been presented in at the AIAA Joint Propulsion Conference by Stanford student Greg Rieker (Publications and AIAA papers #21), in the archival journal Applied Optics (Publication #25), and included in the 2005 JANNAF presentation by Dr. Mark Gruber of AFRL (Presentations at Meetings #16). A third measurement campaign to AFRL to investigate this measurement technology for H₂O concentration and gas temperature is planned for December 2006. The third campaign has three goals: (1) compare the direct absorption sensing strategy used previously with wavelength modulation spectroscopy with 2f detection, (2) transition from experiments to investigate sensor performance for gas temperature to experiments to use gas temperature to study the performance of the scramjet combustor, and (3) investigate the feasibility of measurements of CO₂ near 2μm.

Dr. Jeffries of Stanford participated in a workshop in May 2005 at AFRL organized by Barry Kiel to facilitate diagnostic measurements on augmented jet engines. A joint project with Pratt and Whitney (Jeff Lovett) and AEDC has begun to develop a prototype sensor strategy for measurements in the augmentor of high-performance military gas turbine aeroengines.

During the grant period, the Hanson group had significant interaction with AFRL scientists at Wright-Patterson AFB. For example, in addition to the collaborative measurements in Test Cell 22 at WPAFB, Professor Hanson participated in a workshop at in November, 2005 on plasma stabilized combustion. Dr. Jeffries gave a public talk at AFRL in March 2006 on diode laser sensors for propulsion ground test.

During this period of AFOSR support, Professor Hanson has given invited presentations to several industrial laboratories, universities, and government groups that highlight our progress on AFOSR-sponsored diagnostics research. Members of our group have also provided technical information and advice, by telephone and mail, to several external researchers interested in duplicating or extending our diagnostics concepts.

5.2 Transitions

Significant technical transitions of the combustion diagnostics developed under this program have occurred with several industrial and government scientists during the grant period. This work has primarily focused on the development of practical sensors using the tunable diode laser diagnostic strategies developed over the past decade at Stanford University. These significant technology transitions include:

Customer	Result	Application
Dr. Jeffery Lovett, Pratt and Whitney, East Hartford, CT (860)557-0559	Tunable diode laser diagnostics for gas temperature measurements	Diagnostics of instabilities in augmented aircraft engines

Dr. Michael Aarnio, Pratt and Whitney, Seattle Aerosciences Center (425-450-3930)	Tunable diode laser diagnostics	Use in pulse detonation engine development tests at the Naval Warfare Center at China Lake, CA
Dr. Michael Winter, Pratt and Whitney, East Hartford (860- 565-9007)	Tunable diode laser diagnostics	Development of new sensor for air mass flux for in-flight aero-engine testing; proof-of- concept tests on PW6000 aeroengine July 2005
Dr. Mark Woodmansee, General Electric Global Research Center (518-387- 4220)	Tunable diode laser diagnostics	Potential new sensor for exhaust pattern factor from fixed gas turbines for power generation
Dr. Anthony Dean, General Electric Global Research Center (518-387- 6478)	Tunable NIR and MIR laser diagnostics	Stanford demonstration at GE research laboratories in pulse detonation engine development tests
Dr. Mark Allen PSI Corp Andover, MA (978)689-0003	Gas sensors based on tunable diode lasers using 2f techniques	Temperature sensors for practical industrial applications; sensor for IC- engines developed
Dr. Andrew Sappey Zolo Technologies Boulder, CO (303)604-5800	Wavelength-Multiplexed tunable diode laser sensor strategies	Temperature sensors for practical industrial applications
Dr. Douglas Baer, Los Gatos Research (650 965 7778)	High Pressure Laser- Induced Fluorescence of NO	Gas turbine combustor ground test measurements of NO spatial distributions
Dr. Andrew Sappey, Zolo Technology, (303- 604-5804)	Tunable diode laser diagnostics	Ground test of augmented jet engines and scramjet vehicle health monitoring systems

6.0 New discoveries, inventions, patent disclosures

No patent or invention disclosures.

7.0 Honors/Awards

Professor Ronald K. Hanson was elected Fellow of the ASME during 2004.

The AIAA Best Paper Award for Ground Testing was presented at the 40th JPC in Portland, OR, in June, 2004 to the paper by J.T.C. Liu, J.B. Jeffries, R.K. Hanson, S. Creighton, J.A. Lovett, D.T. Shouse entitled “Diode Laser Absorption Diagnostics for Measurements in Practical Combustion Flow Fields.” This paper, which had been given at the 39th AIAA/ASME/SAE/ASEE Joint Propulsion Conference, Huntsville, Al, July, 2003, included authors from Stanford University, Pratt and Whitney, and the Air Force Research Laboratory.

Lifetime awards of Professor Ronald K. Hanson:

- 1990 Fellow, Optical Society of America (OSA)
Woodard Chair of Mechanical Engineering, Stanford University
- 1996 Aerodynamic Measurement Technology award from the AIAA (first recipient)
- 1997 Fellow, American Institute of Aeronautics and Astronautics (AIAA)
- 2001 Elected to the National Academy of Engineering
- 2002 Silver Medal of the Combustion Institute
- 2004 Fellow, American Society of Mechanical Engineers
- 2005 Propellants and Combustion award from the AIAA